Phase field crystal modeling of grain boundaries

Hult Blixt, Kevin

2025

LUND UNIVERSITY

PHASE FIELD CRYSTAL MODELING OF GRAIN BOUNDARIES

KEVIN HULT BLIXT

Solid Mechanics

Doctoral Thesis

Department of Construction Sciences

Solid Mechanics

ISRN: LUTFD2/TFHF-25/1073-SE(1-186)
ISBN: 978-91-8104-477-5 (print)
ISBN: 978-91-8104-478-2 (pdf)

Phase Field Crystal Modeling of Grain Boundaries

Doctoral Thesis by

Kevin Hult Blixt

Printed by Media-Tryck AB, Lund, Sweden
For information, address:
Division of Solid Mechanics, Lund University, Box 118, SE-221 00 Lund, Sweden
Homepage: www.solid.lth.se

"No man ever wetted clay and then left it,
as if there would be bricks by chance and fortune."
– Plutarch

Contents

Abstract

Grain boundaries (GBs) play a fundamental role in determining the properties of polycrystalline materials, such as metals. However, many of these properties continue to elude precise characterization, both experimentally and computationally. This challenge stem from the small spatial extent of GBs, the wide range of timescales associated with GB-related processes, the strong anisotropy of GB properties and the great structural diversity and variation in GB structures.

To aid in the understanding of these systems, this thesis investigates selected GB properties in bicrystalline systems using the phase field crystal (PFC) method. The PFC approach bridges atomic-scale spatial resolution and diffusive time scales, while naturally incorporating elasticity and plasticity. Compared to other atomistic methods, PFC offers a relatively efficient framework, enabling the systematic exploration of GB behavior.

In this work, the PFC method is employed to sample key GB properties — such as GB energy and migration velocity — as functions of various GB descriptors. Interactions between GBs and second-phase particles (Zener pinning) are also examined. The results highlight the strong anisotropy often observed in GB properties and demonstrate how PFC can serve as an effective tool for investigating the variability of these properties and related processes. Furthermore, PFC results are systematically compared to those obtained from other atomistic methods, such as molecular dynamics, and are found to be in good agreement. Finally, the model is extended to more complex crystal structures — beyond BCC and FCC — with the diamond cubic structure used as a case study, demonstrating the potential of the PFC method for exploring a broader class of crystalline materials.

Popular science summary

Many materials, particularly metals like steel and copper, are composed of a repeating arrangement of atoms known as an atomic lattice. This orderly structure is often disrupted, however, by boundaries that can form during solidification or deformation. A useful analogy is how water freezes on a car windshield during a cold winter day, forming small crystals that grow outward from multiple starting points. As these individual grains expand, each with slightly different orientation, they eventually meet and create grain boundaries — regions where the crystallographic symmetry is interrupted. These grain boundaries play a crucial role in determining the unique properties of metals and other crystalline materials.

This thesis focuses on the study of these grain boundary structures, particularly how they can be explored using a simulation technique known as the phase field crystal (PFC) method. This tool enables simulations at the atomic scale, offering valuable insights into the behavior and properties of materials while enhancing our understanding of their nanoscale structures. Additionally, PFC is efficient enough to simulate atomic phenomena over extended time scales, making it especially useful for studying dynamic processes such as grain growth — a phenomenon where some grains grow larger, while others shrink and are absorbed.

The research presented in this thesis examines both the static and dynamic properties of small sections of single grain boundaries, with an emphasis on the variability of grain boundary properties. Two primary aspects were investigated: grain boundary energy and grain boundary structure. These studies were conducted both to compare PFC results with established data and models, as well as to extend previous research. The findings revealed that PFC simulations closely match existing data. Furthermore, the efficiency of the PFC method allows for the study of a wider range of parameter variability, providing deeper insights into grain boundary behavior.

These investigations are essential, as many larger-scale models, which do not directly incorporate atomic-scale details, often neglect the variability in grain boundary properties. This oversight can impact the accuracy and reliability of their results. The PFC method can serve as a vital link in integrating crystallographic variability into models that depend on external data repositories. By improving these repositories with more comprehensive data, larger-scale models can be enhanced, leading to more accurate and reliable simulations of material behavior at larger scales.

Populärvetenskaplig sammanfattning

Många material, särskilt metaller som stål och koppar, består av ett regelbundet arrangemang av atomer, ett så kallat atomgitter. Denna ordnade struktur avbryts dock ofta av gränser som kan ha bildas under materialets stelning eller deformation. En användbar analogi är hur vatten fryser på en bilruta under en kall vinterdag och bildar små kristaller som växer utåt från flera startpunkter. När dessa individuella kristaller, alla med olika orientering, växer och till slut möts, bildas korngränser. Dessa gränser definierar områden där den kristallografiska symmetrin bryts och spelar en avgörande roll för metallers, och andra kristallina materials, unika egenskaper.

Denna avhandling fokuserar på korngränsstrukturer och hur de kan utforskas med en simuleringsteknik som kallas fasfältskristallmetoden (PFC-metoden). Detta verktyg möjliggör simuleringar på en atomär nivå och ger värdefulla insikter i materialens beteende och egenskaper, samtidigt som förståelsen för nanostrukturer fördjupas. PFC-metoden är dessutom tillräckligt effektiv för att simulera atomära fenomen över längre tidsperioder, vilket gör den särskilt användbar för att studera dynamiska processer såsom korntillväxt — ett fenomen där vissa korn växer sig större medan andra krymper och till slut absorberas.

Forskningen som presenteras i denna avhandling undersöker både de statiska och dynamiska egenskaperna hos enskilda korngränser, med särskilt fokus på variationer i deras struktur och energi. Två centrala aspekter har studerats: korngränsenergi och korngränsstruktur. Undersökningarna genomfördes dels för att jämföra resultaten från PFC-metoden med andra etablerade modeller och dels för att vidareutveckla tidigare forskning. Resultaten visar att PFC-simuleringar stämmer väl överens med befintliga data. Dessutom möjliggör metodens numeriska effektivitet en bredare utforskning av, bland annat, geometriska parametrar, vilket ger fördjupad förståelse för korngränsers beteende.

Dessa typer av undersökningar är viktiga eftersom många storskaliga modeller, som inte direkt inkluderar detaljer på atomär nivå, ofta bortser från variationer i korngränsegenskaper. En sådan förbiseelse kan påverka resultatens noggrannhet och tillförlitlighet. PFC-metoden kan fungera som en viktig länk för att integrera kristallografisk variation i modeller som är beroende av externa databaser. Genom att förbättra dessa databaser med mer omfattande och detaljerad information kan storskaliga modeller utvecklas vidare, vilket i sin tur leder till mer noggranna och tillförlitliga simuleringar av materialbeteende i större skala.

Acknowledgments

They say that you should set your course by the stars, not by the lights of every passing ship. I cannot claim, however, to have set my gaze quite so high. Luckily for me, the ships I chose to follow did not lead me astray. On the contrary, they guided me through stormy weather, pushed me on when the wind was weak and gave me the tools to venture out on my own. Those ships have been my family, friends, teachers and, of course, my supervisor Håkan Hallberg. All to whom I am eternally grateful.

So this is for my family, who have always allowed me to be myself, for better or worse. They have supported me in all my various endeavors, whether building a canoe and sailing down the Helge River or pursuing my engineering degree. Now, as I present this thesis, I am reminded of how they have always been, and continue to be, there for me. So this is to Paul, Therese, Judith, Nathalie and Stefan. Thank you all for being who you are and for everything you do.

I also want to thank my office roommate, Florian Schott, for being such a warm and thoughtful presence — always available to bounce around ideas or head out canoeing when it was time for a break. I would also like to extend my gratitude to Jacob Holmberg-Kasa, not only for carefully reading through this thesis, but also for the many insightful discussions about PFC.

Finally, but certainly not least, I extend my deepest gratitude and indebtedness to my supervisor Håkan. Thank you for presenting this opportunity to me all those years ago, for illuminating a path I had not previously considered as an option. Where would I be today if Mathias had not suggested that I speak to you about a master's project? Either way, I doubt the journey would have been as fun or fulfilling as this one has been. But as all good stories, this one too, must come to an end.

Lund, March 2025
Kevin Hult Blixt

Chapter 1

Introduction

"There is a crack in everything. That's how the light gets in."
– Leonard Cohen

This thesis explores crystalline systems at the atomic scale, with a particular focus on grain boundaries. The study of grain boundaries and their role in material evolution is a fundamental aspect of materials science. Although only a few atoms thick, grain boundaries significantly influence key mechanical and physical properties and processes, including strength, ductility and diffusion [1]. Despite more than a century of research, dating back to the early 20th century [2], many fundamental questions regarding grain boundary behavior remain unresolved and elementary phenomena continue to elude precise characterization.

At its core, the study of crystalline systems involves analyzing atomic packing and the formation of ordered patterns, where atoms tend to arrange themselves in energetically favorable configurations. However, many structural challenges observed at the atomic scale also manifest at larger scales. This was demonstrated by Bragg and Nye in their bubble raft experiment presented in [3], where bubbles suspended on a soap film reproduced features of atomic arrangements and evolution in crystalline materials.

A related analogy is found in hard-sphere models, where steel spheres can be used to represent atoms. These systems encompass the classical problem of sphere packing as well as the study of disordered states such as liquids [4, 5]. When steel spheres are placed in an inclined container, agitated and then allowed to settle — mimicking the process of solidification — a polycrystalline structure may emerge, characterized by regions of differing orientations and relative displacements. A result of this process is shown in Fig. 1.1, where the arrangement of steel spheres forms a 2D crystal structure, exhibiting multiple phases, including triangular and square lattices, along with visible grain boundaries and vacancies.

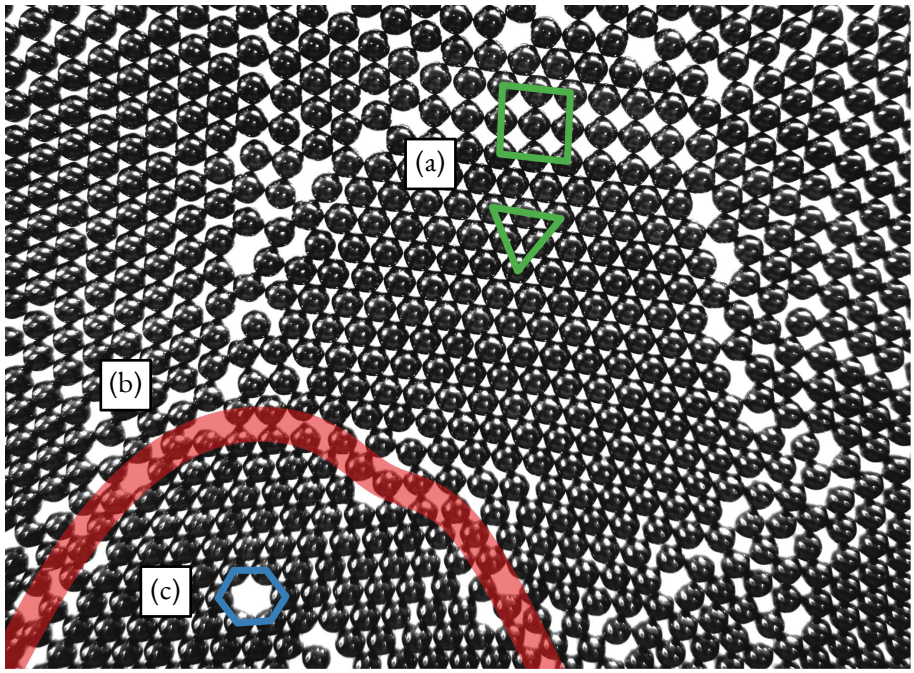

Fig. 1.1: Arrangement of steel spheres illustrating structural features also observed in atomic systems. (a) Shows local packing with triangular and square symmetries, (b) displays a grain boundary separating regions with different orientations and (c) highlights a vacancy in an otherwise ordered lattice.

Just as the hard-sphere models and bubble raft experiments illustrate, atoms also tend to pack and evolve into volumetric efficient configurations. Due to the interatomic potentials between atoms, however, stacking in atomic systems may differ from that of rigid spheres. Nonetheless, the processing history — including crystallization or plastic deformation — often leads to the formation of defects such as grain boundaries, as also observed in Fig. 1.1.

These grain boundaries are associated with a grain boundary, or excess, energy that increases the total energy of the system. If thermodynamic conditions permit, the system may evolve toward a lower-energy configuration by reducing or eliminating these defects. The relevance and motivation for studying grain boundaries and their evolution are discussed further in Chap. 2.

Beyond the fundamental physics and characterization of grain boundaries, this thesis also has a focus on the application of the phase field crystal (PFC) method as a computational framework for their study. Traditional atomistic approaches, such as molecular dynamics (MD) and density functional theory (DFT), provide detailed atomic-scale insights but are constrained by their computational expense, restricting them to short timescales and small domain sizes. MD, for instance, is inherently limited by the atomic vibrational frequency, rendering time scales relevant to grain growth (hours) computationally intractable. Con-

versely, mesoscale methods, such as traditional phase field (PF) modeling, capture long-term material evolution but often rely on simplified representations of atomic-scale phenomena that cannot be readily described through analytical functions.

The PFC method serves as a bridge between these two regimes by preserving atomic-scale spatial resolution while operating on diffusive timescales. This capability makes it an effective tool for investigating grain boundary structures, energy landscapes and dynamic evolution. Further details on the PFC method, its development and mathematical formulations are presented in Chap. 3.

Throughout the appended papers, included at the end of this thesis, we have not only investigated the fundamental physics of grain boundaries but also systematically compared the PFC method with other computational approaches, particularly MD. These comparisons are crucial for validating PFC as a reliable tool for studying real material systems. Although large-scale simulations have not been the primary focus of this work, the validation of grain boundary properties at smaller scales establishes a foundation for future studies, enabling the exploration of grain boundary phenomena at larger scales with increased confidence. A summary of the appended papers, along with future perspectives, is presented in Chap. 4.

Chapter 2

Crystalline systems: Grains and the boundaries that divide them

"God made the bulk; the surfaces were invented by the devil."
– Wolfgang Pauli

A grain boundary is the region at the interface between two abutting crystal grains where a structural mismatch arises due to differences in lattice orientation, displacement or atomic arrangement. This is illustrated in Fig. 2.1, where a region in a metallic material is magnified, first revealing a multitude of crystalline grains with different orientations. These grains can vary significantly in size, with typical widths ranging from the millimeter scale down to just a few nanometers [6]. Larger examples include single crystals produced for use in semiconductors or turbine blades. Upon further magnification, the very thin region separating the grains becomes visible, marking the location of the grain boundary.

This disruption of crystallographic periodicity results in a region with distinct energetic and mechanical properties, with the nature and extent of these variations governed by the specific characteristics of the grain boundary. Despite being microscopic in scale, grain boundaries significantly impact material properties at the macroscopic level and can either enhance or degrade performance depending on their structure and evolution. Specifically, grain boundaries act as barriers to dislocation motion [7], mediate atomic diffusion [8], influence electrical resistivity [9] and affect a range of other mechanical properties.

This chapter will first, in Sec. 2.1, examine the topic of grain growth, introducing key mechanical properties relevant to this thesis. Sec. 2.2 provides a description of atomic lattices, followed in Sec. 2.3, by further details on grain boundary characterization.

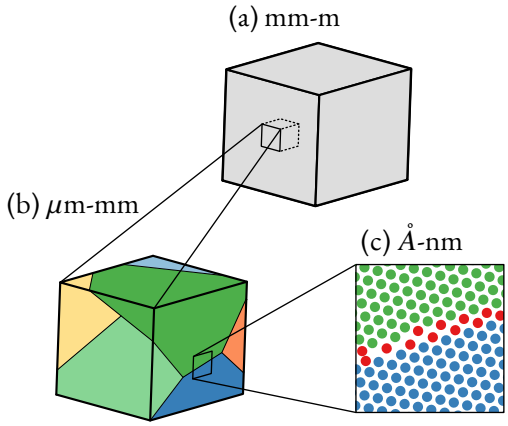

Fig. 2.1: Magnifying a small domain in a piece of metal, as shown in (a), reveals a rich microstructure, seen in (b), where grains with different orientations are separated by thin grain boundaries, highlighted in (c).

2.1 Grain boundary properties and dynamics

The geometric configuration of a grain boundary is fundamental to understanding its properties and behavior. To characterize the grain boundary shown in Fig. 2.1(c), consider the simplified representation in Fig. 2.2. The relative orientation of the crystals in Fig. 2.2 is described by $\theta = \theta_B - \theta_A$, whereas in more general cases, three rotation angles are required. Additionally, two angles define the grain boundary plane normal $\boldsymbol{n}$. Together, these parameters establish the boundary's five macroscopic degrees of freedom (DOF). A more detailed description of grain boundary orientations is provided in Sec. 2.3.

The consideration of these DOFs is essential, as many grain boundary properties — such as grain boundary energy — exhibit strong anisotropy with respect to orientation [2], as also demonstrated in Papers A–C. Interestingly, the variation in grain boundary energy across different metals appears to be largely a matter of scaling [2, 10]. This suggests that insights gained from studying one material with a given crystal structure can be transferred to another material with the same structure. This approach has been applied in Papers A–C to compare PFC results with those obtained from MD simulations.

Furthermore, grain boundary kinetics describe the migration of grain boundaries during grain growth — a process central to the microstructural evolution of polycrystalline materials, such as during the annealing of cold-worked metals. An illustrative example of grain growth is provided in Fig. 2.3, corresponding to the polycrystal presented in Fig. 2.1. Despite the significance of grain boundary migration, the underlying mechanisms that govern it remain only partially understood. This is largely due to the inherent complexity of the process, which occurs at the atomic scale and progresses rapidly at elevated temperatures, making direct experimental observations challenging. Computationally, resolving these processes with

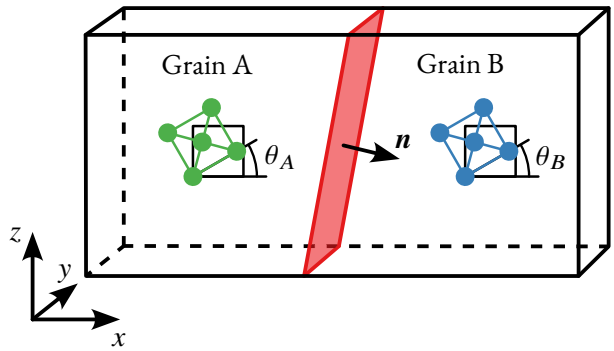

Fig. 2.2: Schematic representation of a grain boundary (shown in red) between two crystalline grains, A and B. The boundary is characterized by the orientations of the grains, θ_A and θ_B, as well as the boundary normal $\boldsymbol{n}$.

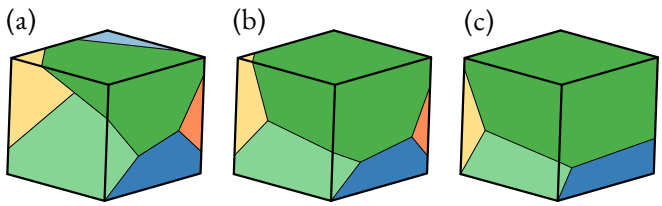

Fig. 2.3: (a)–(c) Illustrative example of grain growth at three consecutive time steps, showing one grain growing at the expense of its neighbors.

both spatial and temporal fidelity is equally demanding, as conventional atomistic methods such as DFT and MD are constrained by their computational cost, as mentioned in Chap. 1.

Although extensive studies have been conducted, both experimentally and through simulations, the results are often contradictory and lack a clear unified pattern, as highlighted in [11]. One of the major challenges in studying grain boundary migration, or any grain boundary-related phenomenon, is the sensitivity of these processes to small perturbations in the system. Even minor modifications, such as the addition of solute atoms, can significantly alter grain boundary properties such as mobility, leading to a complex behavior that can be hard to predict [12]. Even a rough estimate, however, of whether a particular change will increase or decrease grain boundary mobility remains highly beneficial for the design of materials with specific microstructural properties, a field generally referred to as grain boundary engineering [13].

At its core, grain boundary migration arises from the transfer of atoms between adjacent grains — i.e., atomic diffusion — driven by thermodynamic forces that act to minimize the system's free energy. Consider a system composed of two neighboring crystal grains, A and B, separated by a grain boundary, as illustrated in Fig. 2.2. The driving force for boundary motion is then governed by the difference in Gibbs free energy, G, between the grains, which

induces a pressure gradient across the boundary, given by

$$P = -\frac{1}{A}\frac{dG}{dx} \tag{2.1}$$

where A is the area of the grain boundary [11]. This pressure gradient then dictates both the direction and rate of grain boundary migration.

Several mechanisms contribute to the overall grain boundary pressure, each influencing the migration velocity. For example, differences in dislocation density between grains create energy gradients, while capillary forces arising from boundary curvature introduce additional driving pressures [14], as discussed further in Sec. 2.1.1.

2.1.1 Curvature induced grain boundary pressure

The effect of curvature-driven grain boundary pressure was famously investigated by Herring in [15], where he analyzed the energy difference associated with forming a hump on a smoothly curved surface. He found that the local chemical potential, i.e., the change in Gibbs free energy, induces a driving pressure given by

$$P = \kappa_1 \left(\gamma + \frac{\partial^2 \gamma}{\partial \alpha_1^2}\right) + \kappa_2 \left(\gamma + \frac{\partial^2 \gamma}{\partial \alpha_2^2}\right) = \kappa_1 \Gamma_1 + \kappa_2 \Gamma_2 \tag{2.2}$$

where γ is the grain boundary energy, $\kappa_i = 1/R_i$ represents the principal grain boundary curvatures (with R_i denoting the radii of curvature) and α_i are the corresponding grain boundary inclinations. The associated grain boundary stiffness, Γ_i, can be identified from Eq. (2.2) as

$$\Gamma_i(\theta, \boldsymbol{n}) = \gamma(\theta, \boldsymbol{n}) + \frac{\partial^2 \gamma(\theta, \boldsymbol{n})}{\partial \alpha_i^2} \tag{2.3}$$

where θ is the relative rotation between the grains and the grain boundary normal $\boldsymbol{n} = \boldsymbol{n}(\alpha_1, \alpha_2)$ is parameterized using the spherical angles (α_1, α_2). For more general formulations of Eq. (2.2), the reader is referred to [16–18].

It is evident from Eq. (2.2) that determining the driving pressure requires not only knowledge of the grain boundary energy but also its second derivative with respect to the boundary inclination. To incorporate grain boundary stiffness into non-atomistic simulations, analytical functions have been developed and calibrated against large datasets, primarily derived from MD simulations. These include the GB5DOF function, derived in [10] for face-centered cubic (FCC) systems and the uGBE function, developed in [19] for body-centered cubic (BCC) systems. Since both models rely on atomistic simulations using MD, their accuracy depends on the ability to sample a wide range of grain boundary configurations.

Rather than relying directly on the complex analytical functions presented in [10] and [19], some models adopt simplified representations of grain boundary anisotropy [20]. In many cases, however, a constant grain boundary energy is assumed. Under this simplification, and in the 2D case, Eq. (2.2) reduces to

$$P = \kappa\gamma \tag{2.4}$$

As a consequence of its simplicity, Eq. (2.4) naturally neglects many of the underlying physical mechanisms that govern grain boundary behavior. The impact and importance of incorporating anisotropy in simulations have been demonstrated, for example, in [21] for PF simulations and in [22] using the level set method.

2.1.2 Grain boundary mobility

Regardless of the specific form of the driving pressure, if it is sufficiently high, it will induce grain boundary migration. With the migration velocity often assumed to being proportional to the applied driving pressure as

$$v = MP \tag{2.5}$$

where M is the grain boundary mobility parameter. This relationship does not, however, always hold, as additional factors such as temperature, impurity effects and structural anisotropy can significantly influence the final migration rate. Moreover, grain boundary migration is affected by a combination of metastable states, microstructural interactions and crystallographic orientation. Metastable states often inhibit boundary progression, introducing complexities that many existing models struggle to capture due to the lack of analytical expressions describing these conditions. Additionally, microstructural features such as second-phase particles, porosity and solute segregation can further impede boundary motion. These effects, commonly referred to as pinning mechanisms, vary significantly depending on temperature, grain boundary structure and solute concentration. The subject of pinning by second-phase particles was investigated in Paper D.

The influence of grain boundary structure on migration behavior is further complicated by crystallographic orientation. Recent studies suggest that absolute mobility is primarily dictated by the full boundary crystallography rather than the specific driving force applied [23]. This indicates that while thermodynamic driving forces play a role, the underlying atomic structure of the boundary itself is the dominant factor in determining migration behavior. Similar studies to those conducted in [23] were employed in the context of PFC in Paper C.

Finally, it is worth noting that Eq. (2.5) is often combined with Eq. (2.4) to form a simple model of grain boundary migration. In light of recent experimental evidence, however, this linear relationship between grain boundary velocity and curvature appears to be inaccurate, as demonstrated in [24].

2.1.3 Grain boundary stiffness from capillary-wave theory

The grain boundary stiffness, introduced in Eq. (2.2), can be determined using capillary-wave theory. In the approach presented by Buff et al. in [25], the distorted surface of an interface was modeled using a Fourier series to describe equilibrium fluctuations. Their analysis, however, was based on an isotropic fluid with interface energy assumed to be independent of boundary inclination — an assumption that does not hold for metals, as detailed in Sec. 2.1.1.

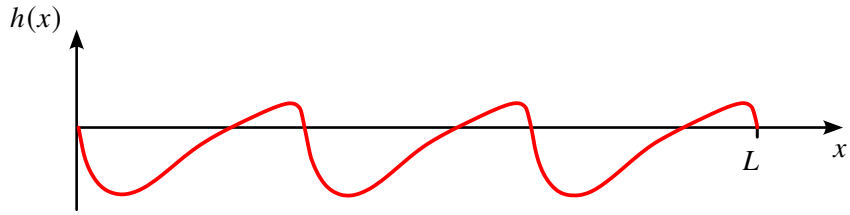

Fig. 2.4: Fluctuating grain boundary profile taken from Paper A, illustrating how the height h varies periodically along the x-direction over a length L.

This limitation was later addressed by Fisher et al. in [26], who introduced the concept of effective interface tension, which takes the same form as the stiffness defined in Sec. 2.1.1.

The capillary-wave theory, later also referred to as the capillary fluctuation method (CFM), has been applied to the study of solid–liquid interfaces, as demonstrated in [27], and solid–solid grain boundaries, as shown in [28]. In CFM, the profile of a quasi-2D interface is considered, such as the one shown in Fig. 2.4, which is taken from Paper A. By analyzing the energy of such a boundary and expressing the contour surface as a Fourier series, it was shown in [27] that the mean square amplitude of the Fourier modes follow as

$$\langle |a(k)|^2 \rangle = \frac{k_B T}{LW\Gamma k^2} \tag{2.6}$$

where k_B is the Boltzmann constant, T is the temperature, L is the grain boundary length, W is the grain boundary width and k is the frequency of the Fourier mode. The stiffness can then be extracted from Eq. (2.6) by analyzing the power spectrum of equilibrium grain boundary profiles, such as the one shown in Fig. 2.4, as a function of k.

It must be noted, however, that Eq. (2.6) was derived under the small-slope approximation ($dh/dx \ll 1$), i.e., for small values of k. Nonetheless, the applicability of Eq. (2.6) has been further confirmed in [28, 29] and was also demonstrated in Paper A to perform well within the context of the PFC method. For a more detailed derivation of Eq. (2.6), the reader is referred to [30].

Finally, it was argued in [27] that calculating Γ is more practical than directly determining γ, owing to the stronger anisotropy of the former. When using MD to compute γ, long averaging times are typically required, rendering its estimation less tractable.

2.2 The atomic lattice

Crystal systems, i.e., the atomic lattice structures, exist in various forms. Cubic systems, such as simple cubic (SC), BCC, FCC and hexagonal close-packed (HCP), are particularly common in metals. The majority of studies presented in this thesis focus on either BCC or FCC structures, as examined in Papers A–D, while Paper D specifically investigates crystals with diamond cubic (DC) lattices.

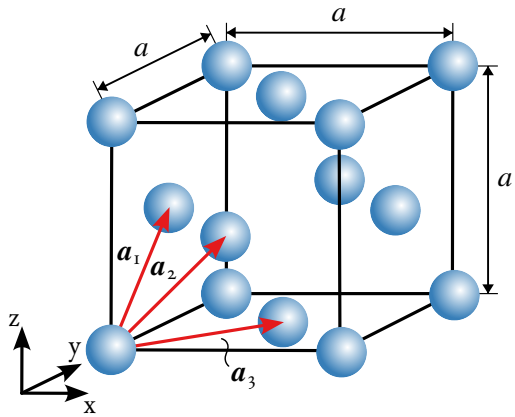

Fig. 2.5: FCC unit cell with a lattice parameter a and its three Bravais lattice basis vectors: $\boldsymbol{a}_1 = a[1/2, 1/2, 0]$, $\boldsymbol{a}_2 = a[1/2, 0, 1/2]$ and $\boldsymbol{a}_3 = a[0, 1/2, 1/2]$.

The rich collection of grain boundary structures arises from the fact that, unlike the rigid spheres shown in Fig. 1.1, atomic systems do not always favor the highest packing factor (atoms per unit volume) arrangements, such as FCC or HCP. Due to factors such as electronic bonding, orbital structure and other interatomic interactions, alternative configurations may exhibit lower energy for specific atomic species [31]. The range of possible structures becomes even broader when considering multi-component systems. Although this represents an important class of materials, the present thesis focuses exclusively on single-component systems.

To describe the atomic arrangement of different systems, the crystallographic structure is typically defined using the Bravais lattice, or direct lattice, with the basis vectors $\boldsymbol{a}_1$, $\boldsymbol{a}_2$ and $\boldsymbol{a}_3$, from which the lattice points are generated as

$$\boldsymbol{R} = n_1\boldsymbol{a}_1 + n_2\boldsymbol{a}_2 + n_3\boldsymbol{a}_3 \tag{2.7}$$

where (n_1, n_2, n_3) are integers. For the FCC lattice, illustrated in Fig. 2.5 using a cubic unit cell, the Bravais lattice basis vectors are given by $\boldsymbol{a}_1 = a[1/2, 1/2, 0]$, $\boldsymbol{a}_2 = a[1/2, 0, 1/2]$ and $\boldsymbol{a}_3 = a[0, 1/2, 1/2]$, where a is the lattice parameter. In some cases, however, the Bravais lattice is decorated with multiple atoms per lattice site. For example, the DC lattice preserves the underlying FCC Bravais lattice but is decorated with two atoms at each lattice point, in contrast to the single atom per point in the FCC structure shown in Fig. 2.5.

2.2.1 Reciprocal Lattice

Instead of describing a system using its Bravais lattice, as given in Eq. (2.7), it is sometimes useful to consider its reciprocal lattice. While the direct lattice describes symmetry points in real space, the reciprocal lattice characterizes symmetry planes in reciprocal space. To formalize this, consider an atomic density field $n(\boldsymbol{r})$, where $\boldsymbol{r}$ denotes a position in space. Assuming

that $n(\boldsymbol{r})$ exhibits the periodicity of the crystal lattice, it can be expressed as a Fourier series of the form

$$n(\boldsymbol{r}) = \sum_m a_m \exp(i\boldsymbol{G}_m \cdot \boldsymbol{r}) \tag{2.8}$$

where a_m are the Fourier coefficients and $\boldsymbol{G}_m$ are the reciprocal lattice vectors. Due to the periodic nature of the lattice, translating $\boldsymbol{r}$ by any lattice vector $\boldsymbol{R}_n$, as described by Eq. (2.7), must yield the same function value, i.e. $n(\boldsymbol{r}) = n(\boldsymbol{r} + \boldsymbol{R}_n)$. Therefore,

$$n(\boldsymbol{r} + \boldsymbol{R}_n) = \sum_m a_m \exp(i\boldsymbol{G}_m \cdot (\boldsymbol{r} + \boldsymbol{R}_n)) = \sum_m a_m \exp(i\boldsymbol{G}_m \cdot \boldsymbol{r}) \exp(i\boldsymbol{G}_m \cdot \boldsymbol{R}_n) \tag{2.9}$$

Since $n(\boldsymbol{r}) = n(\boldsymbol{r} + \boldsymbol{R}_n)$, it follows that $\exp(i\boldsymbol{G}_m \cdot \boldsymbol{R}_n)$ must be unity. This condition is satisfied if

$$\boldsymbol{G}_m \cdot \boldsymbol{R}_n = 2\pi p \tag{2.10}$$

where p is an integer. Assuming that the reciprocal lattice vectors $\boldsymbol{G}_m$ can be written in a form comparable to Eq. (2.7), they take the form

$$\boldsymbol{G}_m = m_1\boldsymbol{b}_1 + m_2\boldsymbol{b}_2 + m_3\boldsymbol{b}_3 \tag{2.11}$$

where (m_1, m_2, m_3) are integers and $(\boldsymbol{b}_1, \boldsymbol{b}_2, \boldsymbol{b}_3)$ are the reciprocal basis vectors. It can then be shown that choosing

$$\boldsymbol{b}_1 = 2\pi \frac{\boldsymbol{a}_2 \times \boldsymbol{a}_3}{\boldsymbol{a}_1 \cdot (\boldsymbol{a}_2 \times \boldsymbol{a}_3)}, \quad \boldsymbol{b}_2 = 2\pi \frac{\boldsymbol{a}_3 \times \boldsymbol{a}_1}{\boldsymbol{a}_1 \cdot (\boldsymbol{a}_2 \times \boldsymbol{a}_3)}, \quad \boldsymbol{b}_3 = 2\pi \frac{\boldsymbol{a}_1 \times \boldsymbol{a}_2}{\boldsymbol{a}_1 \cdot (\boldsymbol{a}_2 \times \boldsymbol{a}_3)}, \tag{2.12}$$

ensures that the orthogonality condition $\boldsymbol{a}_i \cdot \boldsymbol{b}_j = 2\pi\delta_{ij}$ is satisfied [32]. It is worth noting that in crystallographic descriptions, the factor 2π is often omitted, as the convention $\exp(2\pi i\boldsymbol{G}_m \cdot \boldsymbol{R}_n)$ is commonly used instead [32]. Utilizing Eq. (2.12), the reciprocal lattice vectors for the FCC lattice are found as $\boldsymbol{b}_1 = 2\pi[1, 1, -1]$, $\boldsymbol{b}_2 = 2\pi[1, -1, 1]$ and $\boldsymbol{b}_3 = 2\pi[-1, 1, 1]$, which correspond to a BCC lattice in reciprocal space.

2.3 Description and classification of grain boundaries

As mentioned in Sec. 2.1, the characterization of a grain boundary is primarily defined by five macroscopic DOF: three describing the relative orientation between grains and two specifying the orientation of the boundary plane. In addition, three microscopic DOF account for the relative displacement of the adjoining grains. Beyond these geometric descriptors, factors such as grain boundary density, local composition and other atomic-scale variations further contribute to the characterization of grain boundaries. This extended set of DOF, beyond the primary five, leads to a complex grain boundary energy landscape, with grain boundaries exhibiting multiple distinct phases, sometimes referred to as complexions [33, 34]. Some of the commonly used descriptions of crystal orientations and grain boundary characterization are presented in Secs. 2.3.1–2.3.4.

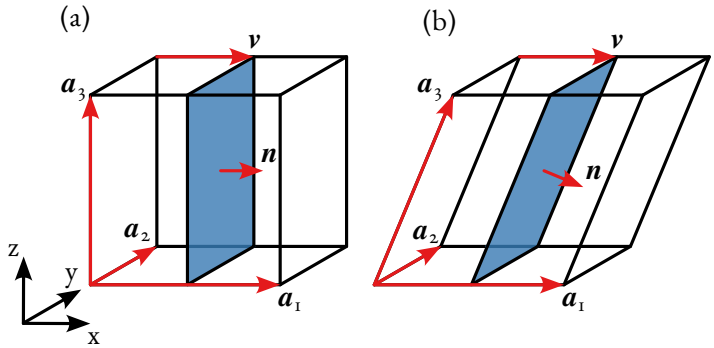

Fig. 2.6: Two unit cells defined by the basis vectors $\boldsymbol{a}_1$, $\boldsymbol{a}_2$ and $\boldsymbol{a}_3$. (a) Represents a cubic lattice, while (b) shows a skewed unit cell forming a parallelogram prism. In both cases, a plane with normal vector $\boldsymbol{n}$ is shown in blue and $\boldsymbol{v}$ denotes a direction vector.

2.3.1 Miller indices

A fundamental step in defining the DOF — particularly those related to orientation — involves describing the crystallographic directions and planes. To this end, Miller indices are commonly used to specify both directions and planes in crystal structures. To illustrate their use, consider the two unit cells shown in Fig. 2.6, each defined by the basis vectors $\boldsymbol{a}_1$, $\boldsymbol{a}_2$ and $\boldsymbol{a}_3$. In this example, Fig. 2.6(a) represents a cubic unit cell, which also describes the FCC unit cell shown in Fig. 2.5, whereas Fig. 2.6(b) depicts a skewed lattice in the form of a parallelogram prism.

Within the Miller index system, directions are described using the smallest integer multiples of the basis vectors, written as $[hkl]$, such that the direction is given by $h\boldsymbol{a}_1 + k\boldsymbol{a}_2 + l\boldsymbol{a}_3$. For both unit cells, the vector $\boldsymbol{v} = 0.5\boldsymbol{a}_1$ and is expressed using Miller indices as $[100]$. When the components are single-digit integers, they are written without commas or spaces and negative values are indicated with an overline, such that $-h = \bar{h}$ [32].

Lattice planes, on the other hand, are described by taking the reciprocals of the plane intercepts along the basis vectors. In both unit cells, the blue plane intersects the $\boldsymbol{a}_1$ axis at $0.5\boldsymbol{a}_1$, while the remaining axes are considered to intersect at infinity. Thus, the Miller indices for both planes are given by $\left(\frac{1}{0.5}\ \frac{1}{\infty}\ \frac{1}{\infty}\right)=(200)$, which is scaled by $1/2$ and written as (100). Here, the use of parentheses indicates that the indices refer to a plane rather than a direction.

The orientation of the plane normal $\boldsymbol{n}$ corresponds to integer multiples of the reciprocal basis vectors, as defined by Eq. (2.12), and is specified by the Miller indices (hkl) such that $\boldsymbol{n} \parallel h\boldsymbol{b}_1 + k\boldsymbol{b}_2 + l\boldsymbol{b}_3$ [35]. In the case shown in Fig. 2.6, both plane normals can be shown to be parallel to $\boldsymbol{b}_1$. A special case arises for cubic lattices, where the reciprocal lattice is also cubic and the basis vectors satisfy $\boldsymbol{a}_i \parallel \boldsymbol{b}_i$. In such cases, the direction $[hkl]$ is perpendicular to the plane (hkl).

Due to lattice symmetry, certain directions or planes exhibit equivalent crystallographic symmetries. For example, in the case shown in Fig. 2.6(a), the (100), (010), (001), ($\bar{1}$00), (0$\bar{1}$0) and (00$\bar{1}$) planes share the same symmetry and belong to the same {100} family of planes. Similarly, the directions [100], [010], [001], [$\bar{1}$00], [0$\bar{1}$0] and [00$\bar{1}$] are part of the same ⟨100⟩ family of directions. These families are indicated by the use of different brackets: {} for equivalent planes and ⟨⟩ for equivalent directions.

2.3.2 Symmetric tilt grain boundaries

In many cases, symmetric boundary types — such as symmetric tilt grain boundaries (STGBs) — simplify the description of grain boundaries, as they exhibit equal but opposite rotations relative to the boundary normal and share a common rotation axis. In the configuration shown in Fig. 2.2, this corresponds to $\theta_A = -\theta_B$. STGBs are typically characterized by their shared tilt axis and by a crystallographic plane that is parallel to the grain boundary plane. For example, a (430)[001] tilt grain boundary refers to a configuration in which the crystallographic plane (430) is parallel to the boundary plane and the common rotation axis [001] is aligned in both grains and lies parallel to the grain boundary plane.

2.3.3 Misorientation

A grain boundary can also be characterized by a misorientation, defined as the rotation required to bring one crystal orientation into alignment with the other. In cases where the two grains share a common rotation axis, the misorientation reduces to a single rotation about that axis, which fully characterizes the relative orientation between the grains. For the configuration illustrated in Fig. 2.2, the misorientation is therefore given by $|\theta_B - \theta_A|$. However, due to the inherent symmetry of the crystal lattice, multiple crystallographic orientations may be considered equivalent. As a result, a smaller rotation angle that yields the same relative crystallographic configuration can often be identified by applying symmetry operations. This minimum-angle rotation is referred to as the disorientation.

2.3.4 Coincident site and displacement shift complete lattices

A special case arises when some of the lattice points of one crystal coincide with those of another. These coincident points form a larger periodic structure known as the coincident site lattice (CSL). An example of a CSL is shown in Fig. 2.7(a), where two square lattices, represented by blue and green circles, share coincident points, highlighted in purple. These coincident points form a larger periodic pattern, illustrated by the square cells connecting the CSL points.

To quantify the degree of coincidence between lattices, the parameter Σ is defined as the ratio of the total number of lattice points to the number of coincident sites within a unit cell of the CSL. In the case shown in Fig. 2.7(a), this value is $\Sigma = 5$. While several studies have attempted to correlate grain boundary energy with lattice coincidence, the Σ value has not

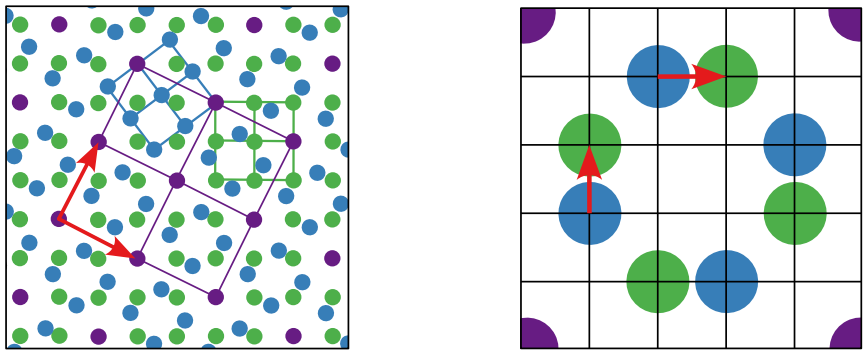

(a) (b)

Fig. 2.7: (a) CSL lattice formed by two square lattices, with atoms shown in green and blue, respectively, and coincident points marked in purple. (b) The corresponding DSC lattice. Shifting one of the lattices by an integer multiple of the displacement vectors (red arrows) in (b) preserves the CSL lattice shown in (a).

proven to be a reliable predictor of grain boundary properties, as also noted for the result presented in Paper B and C [2].

An important property of the CSL is that shifting one of the lattices by a CSL basis vector results in a configuration that preserves lattice coincidence. This is not, however, the smallest possible displacement that maintains coincidence. As illustrated in Fig. 2.7(b), smaller displacement vectors exist that also conserve the CSL structure. These vectors form the displacement shift complete (DSC) lattice, defining the maximum set of lattice shifts required to generate all unique configurations of relative lattice displacements. Notably, distinct defect structures may arise from displacements smaller than those defined by the DSC lattice. The DSC framework thus provides a systematic approach to characterizing grain boundary multiplicities in terms of structure, grain boundary energy and other properties. This approach was employed in Paper B to constrain the search space for possible grain boundary structures, thereby reducing the computational effort required to identify distinct grain boundary configurations.

Chapter 3

Stabilization of periodic phases via the phase field crystal method

"All models are wrong, but some are useful."
– George E.P. Box

The PFC method is a computational framework that enables simulations with atomic-scale spatial resolution while operating on diffusional time scales. Originally developed as an extension of traditional PF models, the PFC formulation has also been shown — under suitable approximations — to be derivable from classical DFT (cDFT) theories [36]. Compared to DFT, the PFC method offers a significant computational advantage by avoiding the need to resolve sharp density peaks, thereby requiring lower spatial resolution. As a result, the PFC model effectively bridges the gap between DFT and conventional PF methods, enabling the study of key physical phenomena in a computationally efficient manner.

The objective of this chapter is to introduce the PFC method for a single-component system. Sec. 3.1 presents the original PFC formulation, which forms the basis for the model used in Paper A. This is followed, in Sec. 3.2, by a discussion on the connection between PFC and cDFT, which provides the foundation for the model introduced in Sec. 3.3 and applied in Papers B–E. Finally, the computational implementation, including a discussion of the spectral method, is presented in Sec. 3.4, concluding this chapter.

3.1 Phase fields and the extension to crystals

The PFC method originates from mean-field theories, including conventional PF models. These models employ order parameters to represent different physical states or properties of a system, such as distinguishing between crystalline and liquid phases [37]. The use of order parameters enables the system's free energy to be expressed in terms of averaged thermodynamic quantities, without explicitly resolving atomic spatial fluctuations.

A key distinction between conventional PF models and the PFC method is that PF models typically involve scalar fields that are spatially uniform in equilibrium. In contrast, the PFC field exhibits periodic spatial variations that reflect the underlying crystal lattice, allowing for the explicit representation of atomic-scale density variations. An example of such a density variation is shown in Fig. 3.1, where the maximum density peak positions have been extracted by interpolation for a subsection of the domain, revealing the FCC crystal structure.

The foundational work on PFC can be traced back to 2002 with the seminal paper by Elder, Katakowski, Haataja and Grant [38]. This development was based on earlier studies of periodic mean field theories, which sometimes employed crystalline terminology, most notably the free energy functional introduced in [39] for the study of convection, nowadays known as the Swift-Hohenberg equation. Drawing inspiration from the Swift-Hohenberg equation, Elder et al. [38] formulated the free-energy functional as

$$F[n(\boldsymbol{r})] = \int_V d\boldsymbol{r} \left\{ n(\boldsymbol{r}) [(q_0^2 + \nabla_{\boldsymbol{r}}^2)^2 - \epsilon] \frac{n(\boldsymbol{r})}{2} + \frac{n(\boldsymbol{r})^4}{4} \right\} \tag{3.1}$$

where the order parameter n represents a conserved density field, $\boldsymbol{r}$ denotes the spatial coordinates and V the volume of the domain. The parameters q_0 and ϵ can be interpreted as material-specific constants. Eq. (3.1) was chosen for its relative simplicity while still being capable of producing periodic states. In [38], it was demonstrated that in 2D, Eq. (3.1) can stabilize a uniform state, a striped phase and, more notably, a hexagonal phase. This hexagonal

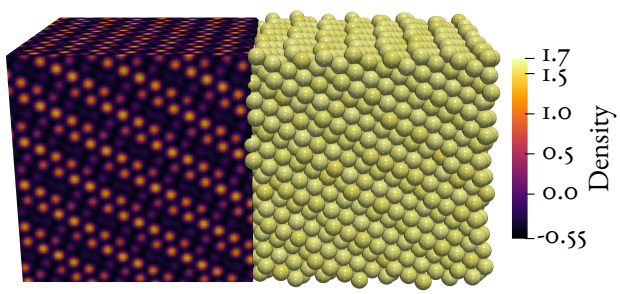

Fig. 3.1: Density field (left) and maximum density peak positions (right) for a density field forming an FCC crystal lattice.

phase exhibits a triangular packing structure, similar to that observed in the {111} crystallographic planes of FCC materials.

To illustrate why and how periodic solutions are stabilized by Eq. (3.1), consider again the Fourier transform of the density field given in Eq. (2.8). As an example, taking the square of this function yields

$$\begin{aligned} n(\boldsymbol{r})^2 &= \sum_{m_1} \sum_{m_2} a_{m_1} a_{m_2} \exp(i \boldsymbol{G}_{m_1} \cdot \boldsymbol{r}) \exp(i \boldsymbol{G}_{m_2} \cdot \boldsymbol{r}) \\ &= \sum_{m_1} \sum_{m_2} a_{m_1} a_{m_2} \exp(i \left(\boldsymbol{G}_{m_1} + \boldsymbol{G}_{m_2} \right) \cdot \boldsymbol{r}) \end{aligned} \tag{3.2}$$

which represents another summation of plane waves, with wave vectors $\boldsymbol{G}_{m_1} + \boldsymbol{G}_{m_2}$, determining the direction and periodicity of the plane waves. For some choices of m_1 and m_2, the condition $\boldsymbol{G}_{m_1} + \boldsymbol{G}_{m_2} = \mathbf{o}$ may hold. This special set of vectors is referred to as the resonant modes, for which the summand remains spatially uniform with a constant value of $a_{m_1} a_{m_2}$.

From Eq. (3.1), it follows that an integration of Eq. (3.2) should be performed. Integrating Eq. (3.2) over a finite volume V that exactly matches the periodicity of the density field n yields

$$\begin{aligned} &\int_V d\boldsymbol{r} \sum_{m_1} \sum_{m_2} a_{m_1} a_{m_2} \exp(i \left(\boldsymbol{G}_{m_1} + \boldsymbol{G}_{m_2} \right) \cdot \boldsymbol{r}) \\ &= V \sum_{m_1} \sum_{m_2} a_{m_1} a_{m_2} \ \forall \ (m_1, m_2) \text{ such that } \boldsymbol{G}_{m_1} + \boldsymbol{G}_{m_2} = \mathbf{o} \end{aligned} \tag{3.3}$$

from which it is evident that, for this specific choice of V, only the resonant terms contribute. In cases where the integration volume does not precisely match the periodicity of n, the resonant modes still scale linearly with V, while the non-resonant (oscillatory) terms — for which $\boldsymbol{G}_{m_1} + \boldsymbol{G}_{m_2} \neq \mathbf{o}$ — fluctuate around zero due to phase cancellation.

In the general case of integrating n raised to the i'th power over a periodic volume, the integral evaluates to

$$\int_V d\boldsymbol{r} n(\boldsymbol{r})^i = V \sum_m a_m \ \forall \ m \text{ such that } \boldsymbol{G}_m = \mathbf{o} \tag{3.4}$$

where $m = (m_1, \ldots, m_i)$ and $\boldsymbol{G}_m = \boldsymbol{G}_{m_1} + \cdots + \boldsymbol{G}_{m_i}$. This demonstrates that the i'th power of the density field is particularly sensitive to resonant modes of order i and that these resonant modes dominate the contributions to the free energy.

Moreover, the zero mode, $\boldsymbol{G}_0 = \mathbf{o}$, can combine with lower-order resonant modes and therefore also appears in higher-order terms if its amplitude satisfies $a_0 \neq 0$. For example, the third-order resonant condition $\boldsymbol{G}_{m_1} + \boldsymbol{G}_{m_2} + \boldsymbol{G}_0 = \mathbf{o}$ includes the second-order resonant mode $\boldsymbol{G}_{m_1} + \boldsymbol{G}_{m_2} = \mathbf{o}$. Together, they contribute to a spatially uniform density field with an amplitude of $a_{m_1} a_{m_2} a_0$. Since a_0 corresponds to the mean density, this provides a mechanism by which the energy of different phases can be controlled through the average density.

Returning to Eq. (3.1), it is now evident that this formulation is sensitive to resonant modes of the second and fourth degrees, as well as the third degree for nonzero mean density. While the resonant modes determine the angular dependence of the periodic phases, the length scale is governed by the linear operator $[(q_0^2 + \nabla_{\boldsymbol{r}}^2)^2 - \epsilon]$. To understand this formulation, consider a two-point correlation function $C_2(\boldsymbol{r}_1, \boldsymbol{r}_2)$, which relates two points, $\boldsymbol{r}_1$ and $\boldsymbol{r}_2$, in the density field and acts as a potential function for interactions. Assuming rotational invariance, this function depends only on the distance r between the points, such that $C_2(\boldsymbol{r}_1, \boldsymbol{r}_2) = C_2(|\boldsymbol{r}_1 - \boldsymbol{r}_2|) = C_2(r)$. Since the Fourier transform of a radially symmetric function is also radially symmetric, as shown in [40], the Fourier transform of $C_2(r)$ is denoted as $\hat{C}_2(k)$, where $k = |\boldsymbol{k}|$. Expanding $\hat{C}_2(k)$ in a Taylor series to fourth order around $k = 0$ yields

$$\hat{C}_2(k) = \hat{c}_0 + \hat{c}_2 k^2 + \hat{c}_4 k^4 \tag{3.5}$$

where odd-order terms are omitted, as their inclusion would introduce directional dependence in the free energy, violating rotational symmetry [37, 41]. In real space Eq. (3.5) transforms to

$$C_2(\boldsymbol{r}) = \left(\hat{c}_0 - \hat{c}_2 \nabla_{\boldsymbol{r}'}^2 + \hat{c}_4 \nabla_{\boldsymbol{r}'}^4\right) \delta(\boldsymbol{r} - \boldsymbol{r}') \tag{3.6}$$

where the gradients are taken with respect to $\boldsymbol{r}'$ [36]. By rearranging Eq. (3.6), it follows that if $\hat{c}_0 = q_0^4 - \epsilon$, $\hat{c}_2 = -2q_0^2$ and $\hat{c}_4 = 1$, then

$$C_2(\boldsymbol{r}) = [(q_0^2 + \nabla_{\boldsymbol{r}'}^2)^2 - \epsilon]\delta(\boldsymbol{r} - \boldsymbol{r}') \tag{3.7}$$

which is the same as in Eq. (3.1) and its reciprocal $\hat{C}_2(\boldsymbol{k})$ is shown in Fig. 3.2 for $q_0 = 1$. For this choice, $\hat{C}_2(\boldsymbol{k})$ exhibits a minimum at $k = 1$, effectively setting the characteristic length scale of the emergent phases. These considerations reveal that the quadratic term in Eq. (3.1) is not only sensitive to the second-order resonant mode but also has its amplitudes weighted by Eq. (3.5). Furthermore, the three quantities $\hat{c}_0$, $\hat{c}_2$ and $\hat{c}_4$ in Eq. (3.5) not only determine

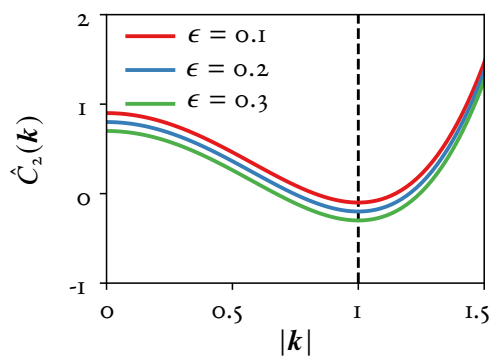

Fig. 3.2: Plot of Eq. (3.5) using $\hat{c}_0 = q_0^4 - \epsilon$, $\hat{c}_2 = -2q_0^2$, $\hat{c}_4 = 1$ and $q_0 = 1$. The function is shown for three different values of ϵ, each exhibiting a minimum at $|\boldsymbol{k}| = 1$, which remains independent of the value of ϵ.

the lattice parameter of the periodic phase but can also be related to the bulk modulus of the crystal [36]. The elastic effects of Eq. (3.7) are discussed further in Sec. 3.1.1. To analyze the emergent phases described by Eq. (3.1) in more detail, the phase diagram is constructed in Sec. 3.1.2.

Finally, it is noted that with the correlation function presented in Eq. (3.7), a triangular phase can be stabilized in 2D, while a BCC phase can be stabilized in 3D. For other crystal phases, such as FCC, additional modes must be included, which can be achieved by considering higher-order terms in the Taylor expansion in Eq. (3.5). Details on such correlation functions are presented in Paper A. A different type of correlation function, also capable of stabilizing FCC, is utilized in Papers B–D and is discussed in Sec. 3.3. For extensions to more complex models capable of stabilizing, for example a DC phase, the reader is directed to Paper E.

3.1.1 Elasticity

Although elasticity is not explicitly treated in the appended papers, it is implicitly accounted for through the evaluation of grain boundary energy in Papers A–C, making it a relevant consideration. To demonstrate how elastic effects are incorporated in Eq. (3.1), consider a simple 1D example where the density variation can be represented by a sinusoidal function, given by $n(x) = a\sin(qx)$, where q denotes the wavenumber. Assuming the energy is minimized at $q = q_0$, a strained configuration can be represented by $q = q_0(1+\beta)$, where β denotes the strain.

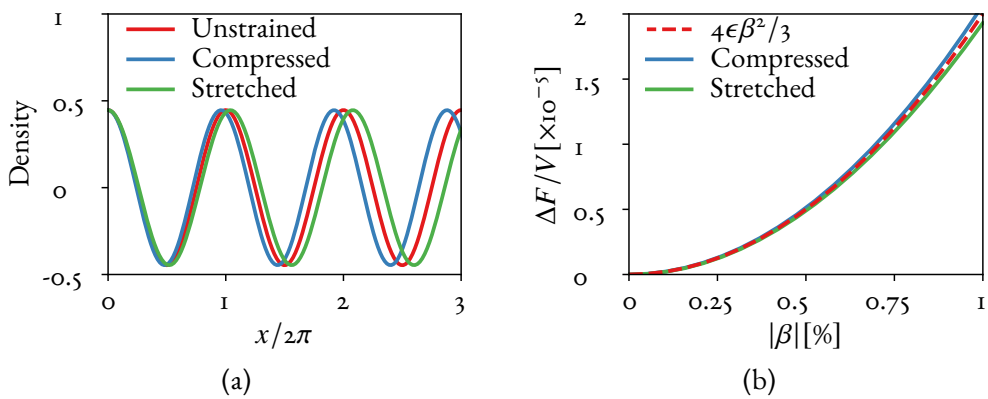

Fig. 3.3: Evaluation of strain-induced energy variation for a 1D periodic phase. (a) The density field for a unstrained, compressed and stretched state, where the strain has been amplified by a factor of four to enhance visibility. (b) The mean energy difference from the unstrained state as a function of the strain magnitude $|\beta|$. The simulation results are compared with the analytical model given in Eq. (3.8) for $\epsilon = 0.15$.

The mean energy variation away from equilibrium, ΔF, is obtained from Eq. (3.1) by integrating over a periodic domain. By setting $q_0 = 1$ and assuming $\beta \ll 1$, the resulting elastic strain energy per unit volume appear as

$$\frac{\Delta F}{V} = \frac{4}{3}\epsilon\beta^2 \tag{3.8}$$

which is consistent with the standard quadratic form characteristic of linear elastic materials. The elastic modulus is then determined by the second derivative of Eq. (3.8) with respect to β, yielding a value of $8\epsilon/3$. Consequently, the parameter ϵ directly governs the elastic modulus.

The energy can also be evaluated numerically, as shown in Fig. 3.3 for $\epsilon = 0.15$ and $q_0 = 1$. Figure 3.3(a) shows a portion of the density field for the initial (unstrained) configuration, as well as for the largest negative (compressed) and positive (stretched) strain states. The strains have been scaled by a factor of four to enhance visibility. The corresponding energy as a function of strain is presented in Fig. 3.3(b), along with the analytical model given in Eq. (3.8). As shown, Eq. (3.8) provides a good fit for small values of β.

3.1.2 Phase diagram

To identify suitable model parameters, it is often helpful to examine the phase diagram. To this end, two main approaches are commonly used for its construction: either by directly minimizing Eq. (3.1) or, as done here, by assuming a few reasonable phases, optimizing their amplitudes and comparing their energies. For Eq. (3.1), it is assumed that the system either has a constant phase, $n_c(x, y) = a_0$, a striped phase

$$n_s(x, y) = a_0 + a_s \sin(q_s x) \tag{3.9}$$

or a triangular phase,

$$n_t(x, y) = a_0 + a_t \left[\cos(q_t x)\cos(q_t y/\sqrt{3}) + \frac{1}{2}\cos(2q_t y/\sqrt{3})\right] \tag{3.10}$$

where a_0 is the mean density, which is typically user-defined and used to control the active phase. The density fields corresponding to the striped and triangular phases are shown in Fig. 3.4. The associated density planes are also illustrated, highlighting the direction of the reciprocal lattice vectors. While the striped phase exhibits a single density plane, the triangular phase displays three distinct planes.

By inserting these low-mode density approximations into Eq. (3.1), the free energy is then determined by integration over a periodic volume V. Setting $q_0 = 1$, the mean free energy for the constant phase is given by

$$\frac{F_c}{V} = (1 - \epsilon)\frac{a_0^2}{2} + \frac{a_0^4}{4} \tag{3.11}$$

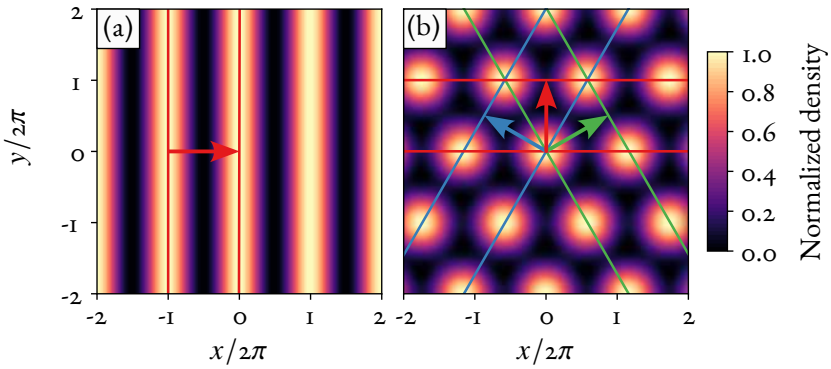

Fig. 3.4: (a) Striped and (b) triangular phases, defined according to Eqs. (3.9) and (3.10), respectively. The relationship between the density planes and the directions of the corresponding reciprocal lattice vectors is also illustrated.

Setting $q_s = 1$ for the striped phase ensures that its period matches the minimum of $\hat{C}_2$, as seen in Fig. 3.2. With this choice of q_s, the mean free energy takes the form

$$\frac{F_s}{V} = \frac{F_c}{V} + \frac{3a_0^2 - \epsilon}{4} a_s^2 + \frac{3}{32} a_s^4 \tag{3.12}$$

From Eq. (3.12), it is evident that the free energy is reduced to that of the constant phase when $a_s = 0$. For the triangular phase the minimum occurs at $q_t = \sqrt{3}/2$, which ensures that the magnitudes of the reciprocal lattice vectors are equal to unity, as illustrated in Fig. 3.4(b). With this choice, the free energy for the triangular phase is given by

$$\frac{F_t}{V} = \frac{F_c}{V} + \frac{9a_0^2 - 3\epsilon}{16} a_t^2 + \frac{3a_0}{16} a_t^3 + \frac{45}{512} a_t^4 \tag{3.13}$$

The phase diagram is constructed using the common tangent construction. This process is illustrated in Fig. 3.5 for two hypothetical phases, 1 and 2. The free energies of the two phases, as functions of the mean density, are shown by the blue and green curves. For $a_0 \leq a_1$, the system remains entirely in phase 1, whereas for $a_0 \geq a_2$, it is entirely in phase 2. In the intermediate region, where $a_1 < a_0 < a_2$, the system energy can be lowered by decomposing into a mixture of phases 1 and 2. The lowest possible system energy in this range corresponds to the convex hull of the two free energy curves, shown by the red dashed line in Fig. 3.5. This convex hull is constructed by identifying the common tangent, represented by the black solid line in Fig. 3.5. The linear segment of this tangent, known as the coexistence line, defines a region in which the system separates into domains of both phases, with mean densities a_1 and a_2, respectively, in proportions that preserve the overall mean density.

To illustrate how the common tangent construction is used in practice to generate the phase diagram, consider again Eqs. (3.11)–(3.13). For a given value of ϵ, the corresponding

tangent points are computed. This process is illustrated in Fig. 3.6(a), showing the coexistence between striped–triangular and triangular–constant phases. Repeating this procedure for multiple values of ϵ allows construction of the full phase diagram, shown in Fig. 3.6(b), where the coexistence regions are highlighted in blue. The resulting diagram can then be used to select values of a_0 and ϵ that yield the desired phase or phases.

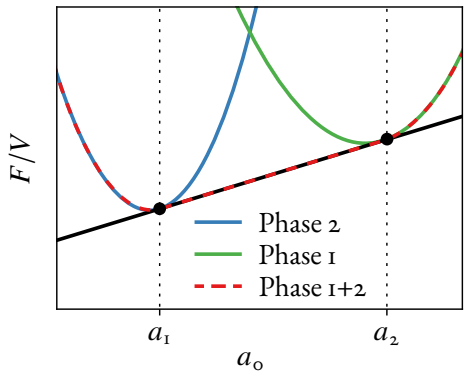

Fig. 3.5: Common tangent construction for two hypothetical phases 1 and 2. At the coexistence line, represented by the linear section between a_1 and a_2, the two phases coexist by decomposing the domain into regions of phase 1 with mean density a_1 and regions of phase 2 with mean density a_2. This decomposition reduces the total energy to the convex hull of the free energy curves, shown by the red dashed line.

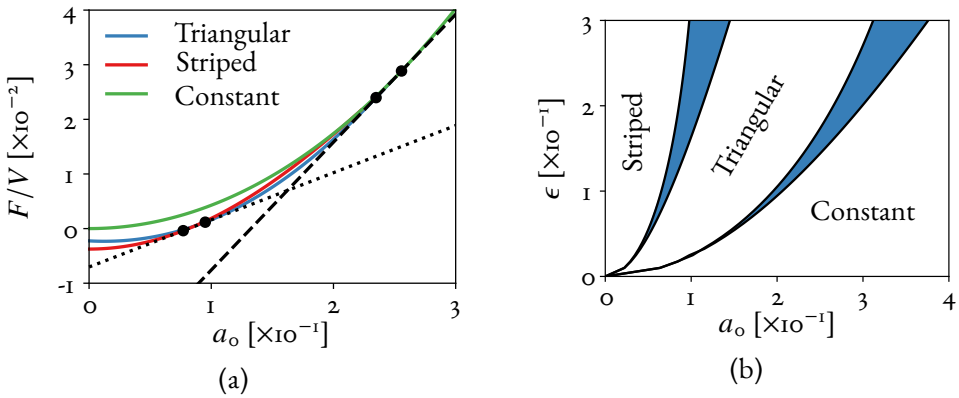

Fig. 3.6: (a) Common tangent construction for Eqs. (3.11)–(3.13) with $\epsilon = 0.15$. Common tangents for the striped–triangular and triangular–constant phases are shown by the dotted and dashed lines, respectively. (b) Resulting phase diagram with coexistence regions in blue.

3.1.3 Modeling of dynamics

Usually, the objective is not simply to minimize the free energy, such as in Eq. (3.1), as this would yield a domain consisting of a single, defect-free phase. Instead, the focus is often on the evolution of defect structures and metastable states, particularly in the context of grain growth. To mimic atomic-scale diffusive dynamics, the density field is evolved using conserved dissipative dynamics. Starting from the continuity equation, the time evolution is governed by

$$\frac{\partial n}{\partial t} = -\nabla \cdot \boldsymbol{j}, \tag{3.14}$$

where $\boldsymbol{j}$ denotes the mass flux. The driving force for diffusion in the system can be expressed as

$$\boldsymbol{j} = -\nabla \Phi \tag{3.15}$$

where Φ is a general scalar potential field [42]. In the case of Fick's first law, this potential corresponds to the concentration, making the flux proportional to the concentration gradient. In the PFC framework, however, this potential is instead given by the chemical potential μ, leading to

$$\boldsymbol{j} = -M \nabla \mu \tag{3.16}$$

where M is the mobility coefficient. Assuming a constant mobility coefficient and substituting Eq. (3.16) into Eq. (3.14) yields

$$\frac{\partial n}{\partial t} = M \nabla \cdot \nabla \mu = M \Delta \mu \tag{3.17}$$

The chemical potential is equal to the functional derivative of the free energy [37], leading to the final evolution equation for the density field as

$$\frac{\partial n}{\partial t} = M \Delta \frac{\delta F}{\delta n} \tag{3.18}$$

This differs from the approach used in the Swift-Hohenberg case in [39], where

$$\frac{\partial n}{\partial t} = \frac{\delta F}{\delta n} \tag{3.19}$$

which is of a nonlocal form and does not correspond to atomic diffusion. Additionally, alternative forms of the time evolution equation have been proposed, including those incorporating second-order derivatives to capture dynamics on different time scales [43–45]. In some cases, a stochastic noise term is also added to Eq. (3.18) to account for thermal fluctuations and to facilitate nucleation [37].

Inserting Eq. (3.1) into Eq. (3.18) yields an evolution equation for the system. This formulation can then be used to study, for example, the growth of a solid phase into a liquid region, as demonstrated for a BCC phase in Fig. 3.7. From Fig. 3.7(a) to Fig. 3.7(b), the progression

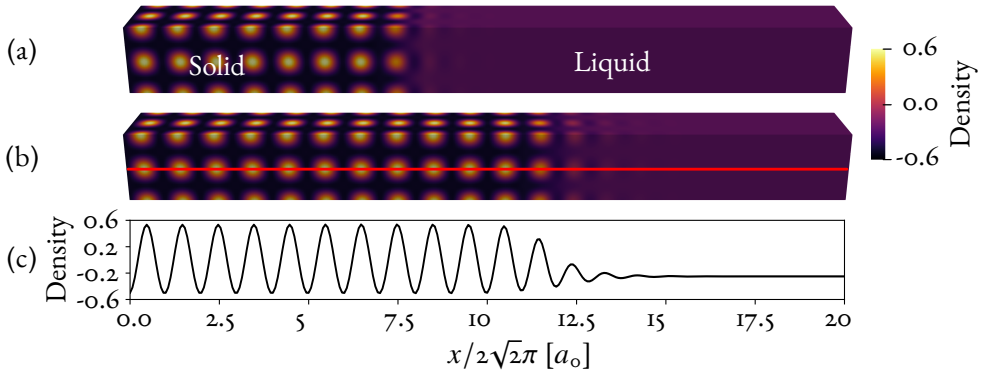

Fig. 3.7: (a)–(b) Crystal growth of a BCC crystal phase into a liquid region at two consecutive time steps. The evolution is determined by Eq. (3.1) and Eq. (3.18), with parameters $a_0 = -0.25$ and $\epsilon = 0.2$, in accordance with the phase diagram in [46]. The density field along the red line indicated in (b) is shown in (c), highlighting the diffuse solid–liquid transition.

of crystal growth is clearly visible. The density along the line indicated in Fig. 3.7(b) is shown in Fig. 3.7(c). The resulting profile illustrates the transition from solid to liquid, revealing that the interface is diffuse rather than sharp.

As a final demonstration, a density field is initialized with small crystalline seeds that are allowed to grow into the surrounding liquid region, as shown in Fig. 3.8. By the end of the simulation, grain boundaries have formed, consisting of dislocations, as illustrated in Fig. 3.8(d). Further details on the implementation of the spectral method used to evolve the density field are provided in Sec. 3.4.

3.2 Free energy functionals and their connection to density functional theory

The previous section approached the PFC free energy functional from a mathematical perspective. However, as mentioned in the introduction, connections exist between PFC and more physically motivated models, such as DFT. Due to the necessary simplifications of the DFT equations, obtaining accurate physical properties from PFC free energy functionals, whether of the Swift-Hohenberg type or others, has proved challenging. Nevertheless, deriving PFC from cDFT provides a conceptual framework for interpreting the variables present in the free energy functional.

In general, cDFT postulates that the free energy of a system is a functional of its density. The Helmholtz free energy is typically expressed as the sum of the ideal gas energy, F_{id}, and

an excess energy term, F_{exc}, following

$$F\left[\rho(\boldsymbol{r})\right] = F_{id}\left[\rho(\boldsymbol{r})\right] + F_{exc}\left[\rho(\boldsymbol{r})\right] \tag{3.20}$$

where ρ is the one-body density distribution [47]. The ideal gas energy represents the free energy of a non-interacting system and is given by

$$F_{id}[\rho(\boldsymbol{r})] = k_B T \int d\boldsymbol{r}\rho(\boldsymbol{r}) \left\{\ln\left[\Lambda_T^3 \rho(\boldsymbol{r})\right] - 1\right\} \tag{3.21}$$

where Λ_T is the thermal de Broglie wavelength [48]. The second term in Eq. (3.20), the excess free energy, accounts for interparticle interactions [47]. The excess energy can be expanded in a functional Taylor series around a reference liquid density ρ_{ref}, following [49], as

$$F_{exc}[\rho(\boldsymbol{r})] = F_{exc}[\rho_{ref}] + \sum_{n=1}^{\infty} \frac{1}{n!} \int \left.\frac{\delta^n F_{exc}[\rho(\boldsymbol{r})]}{\prod_{i=1}^{i=n} \delta\rho(\boldsymbol{r}_i)}\right|_{\rho_{ref}} \prod_{i=1}^{n} \Delta\rho(\boldsymbol{r}_i) d\boldsymbol{r}_i \tag{3.22}$$

where $\Delta\rho(\boldsymbol{r}_i) = \rho(\boldsymbol{r}) - \rho_{ref}$. The n-point direct correlation function C_n is then defined as

$$C_n(\boldsymbol{r}_1, ..., \boldsymbol{r}_n) \equiv -\frac{1}{k_B T} \left.\frac{\delta^n F_{exc}[\rho(\boldsymbol{r})]}{\prod_{i=1}^{i=n} \delta\rho(\boldsymbol{r}_i)}\right|_{\rho_{ref}} \tag{3.23}$$

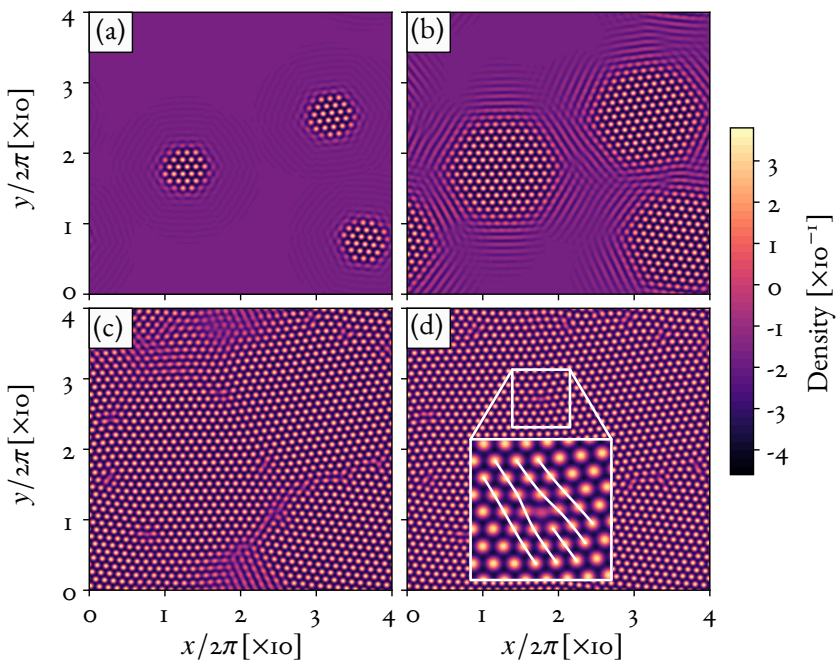

Fig. 3.8: (a)–(d) The evolution of small crystalline grains exhibiting triangular phases, simulated using Eq. (3.1) with $\epsilon = 0.1$ and $a_0 = -0.15$, over linearly spaced time steps. In (d), dislocations are visible at the interfaces between grains, forming the grain boundaries.

and describes the potential energy of interactions between particles [36, 49]. Substituting Eq. (3.23) into Eq. (3.22) allows the latter to be rewritten as

$$F_{exc}[\rho(\boldsymbol{r})] = F_{exc}[\rho_{ref}] - k_B T \sum_{n=1}^{\infty} \frac{1}{n!} \int C_n(\boldsymbol{r}_1, ..., \boldsymbol{r}_n) \prod_{i=1}^{n} \Delta\rho(\boldsymbol{r}_i) d\boldsymbol{r}_i \tag{3.24}$$

Combined with the formulation for the ideal gas energy, Eq. (3.21), the free energy takes the form

$$\begin{aligned} F[\rho(\boldsymbol{r})] = k_b T \int d\boldsymbol{r} \rho(\boldsymbol{r}) \left\{ \ln\left[\Lambda^3 \rho(\boldsymbol{r})\right] - 1 \right\} + F_{exc}(\rho_{ref}) \\ - k_b T \sum_{n=1}^{\infty} \frac{1}{n!} \int \prod_{i=1}^{n} d\boldsymbol{r}_i C_n(\boldsymbol{r}_1, ..., \boldsymbol{r}_n) \Delta\rho(\boldsymbol{r}_i) \end{aligned} \tag{3.25}$$

To ensure that the free energy remains invariant under translations and rotations, C_1 must be a constant and is typically set to zero [49]. Following the approach in [50], Eq. (3.25) is typically truncated at C_2. Higher-order terms may be retained, however, to stabilize more complex crystal structures—as shown for a DC crystal in Paper E. Furthermore, the integrand of F_{id} is also expanded in a Taylor series around ρ_{ref}, following

$$\begin{aligned} \rho \ln(\Lambda^3 \rho) - \rho \approx \rho_{ref} \ln\left(\Lambda^3 \rho_{ref}\right) - \rho_{ref} + \\ \rho_{ref} \left[\ln\left(\Lambda^3 \rho_{ref}\right) n + \frac{1}{2} n^2 - \frac{1}{6} n^3 + \frac{1}{12} n^4 + O(n^5) \right] \end{aligned} \tag{3.26}$$

where the reference to $\boldsymbol{r}$ has been omitted for brevity and the dimensionless variable $n = (\rho - \rho_{ref})/\rho_{ref}$ has been introduced. It is to be noted that although n has been used to denote the normalized density field here and in Sec. 3.1, Papers A and D use a different notations as a consequence of the varying conventions in the literature. The variation in notation between the appended papers is further discussed in Sec. 4.3.

By combining Eq. (3.25), truncated at C_2, with Eq. (3.26), the resulting expression for the free energy becomes

$$\begin{aligned} F[n] = & F_{id}[\rho_{ref}] + F_{exc}[\rho_{ref}] + \\ & k_B T \rho_{ref} \int d\boldsymbol{r} \left[\ln\left(\Lambda^3 \rho_{ref}\right) n + \frac{1}{2} n^2 - \frac{1}{6} n^3 + \frac{1}{12} n^4 \right] - \\ & \frac{k_B T \rho_{ref}^2}{2} \int d\boldsymbol{r}_1 d\boldsymbol{r}_2 n(\boldsymbol{r}_1) C_2(\boldsymbol{r}_1, \boldsymbol{r}_2) n(\boldsymbol{r}_2) \end{aligned} \tag{3.27}$$

where $\Delta\rho = \rho_{\text{ref}} n$ has been used. Following the approach in Sec. 3.1, the two-point correlation function is assumed to be isotropic, such that $C_2(\boldsymbol{r}_1, \boldsymbol{r}_2) = C_2(|\boldsymbol{r}_2 - \boldsymbol{r}_1|) = C_2(r)$. Furthermore, constant terms and the term linear in n are typically neglected [49]. With these simplifications, Eq. (3.27) can be restated as

$$\frac{F[n]}{k_B T \rho_{ref}} = \int d\boldsymbol{r} \left(\frac{\zeta_1}{2} n^2 - \frac{\zeta_2}{6} n^3 + \frac{\zeta_3}{12} n^4 \right) - \frac{1}{2} \int d\boldsymbol{r}_1 d\boldsymbol{r}_2 n(\boldsymbol{r}_1) C_2(r) n(\boldsymbol{r}_2) \tag{3.28}$$

where the parameters $(\zeta_1, \zeta_2, \zeta_3)$ have been introduced and ρ_{ref} has been absorbed into C_2. Eq. (3.28) represents the standard form of the free energy functional used in many PFC implementations. From this expression, various formulations of the PFC model can be derived, including the Swift-Hohenberg equation introduced in Eq. (3.1). An alternative model, employed in Papers B–D, will be discussed next in Sec. 3.3.

3.3 The structural phase field crystal method

The structural PFC (XPFC) method was introduced in [51], drawing inspiration from DFT and the free energy functional given in Eq. (3.28). In contrast to the Swift-Hohenberg formulation in Eq. (3.1), which is limited to a fourth-order polynomial in Fourier space, the two-point correlation function in XPFC is defined as a sum of Gaussian peaks.

As a starting point for constructing the XPFC correlation function, consider a perfect crystal at finite temperature, where atoms vibrate about their lattice sites. Assuming that atomic positions follow a Gaussian probability distribution, the probability density field ρ in a 1D case can be written as

$$\rho(x) = \sum_m \rho_m(x) = \sum_m \frac{1}{\sqrt{2\pi\sigma_v^2}} e^{-\frac{(x-x_m)^2}{2\sigma_v^2}} \tag{3.29}$$

where σ_v represents the vibrational amplitude of the atoms and x_m is the position of the m'th atom [52]. The Fourier transform of Eq. (3.29) is then evaluated as

$$\mathcal{F}[\rho(x)](k) = \hat{\rho}(k) = \frac{1}{\sqrt{2\pi\sigma_v^2}} \sum_m \int_{-\infty}^{\infty} e^{-\frac{(x-x_m)^2}{2\sigma_v^2}} e^{-ikx} dx \tag{3.30}$$

where $\mathcal{F}[\rho]$ denotes the Fourier transform of ρ. Using the shift property of the Fourier transform, $\mathcal{F}\{g(x-a)\} = \mathcal{F}\{g(x)\} e^{-ika}$, the Fourier transform of a Gaussian centered at x_m is given by

$$\mathcal{F}[e^{-\alpha(x-x_m)^2}](k) = \sqrt{\frac{\pi}{\alpha}} e^{-\frac{k^2}{4\alpha}} e^{-ikx_m} \tag{3.31}$$

where $\alpha = 1/(2\sigma_v^2)$ has been introduced [53]. Thus, Eq. (3.30) appears as

$$\hat{\rho}(k) = e^{-\frac{\sigma_v^2 k^2}{2}} \sum_m e^{-ikx_m} \tag{3.32}$$

As a 1D case is considered here, the lattice positions are given by $x_m = am$, where a is the lattice spacing, i.e., the lattice parameter. With this in mind, the sum in Eq. (3.32) can be identified as the Fourier series representation of the Dirac comb function, such that

$$\sum_{m=-\infty}^{\infty} e^{-ikx_m} = \sum_{m=-\infty}^{\infty} e^{-ikam} = \frac{2\pi}{a} \sum_{m=-\infty}^{\infty} \delta(k - \frac{2\pi m}{a}) \tag{3.33}$$

as shown, for example, in [53]. Substituting Eq. (3.33) into Eq. (3.32) yields

$$\hat{\rho}(k) = e^{-\frac{\sigma_v^2 k^2}{2}} \frac{2\pi}{a} \sum_{m=-\infty}^{\infty} \delta(k - \frac{2\pi m}{a}) \tag{3.34}$$

which thus represents a series of δ-peaks corresponding to the periodic planes of the crystal lattice. The pre-factor $e^{-\sigma_v^2 k^2/2}$ causes the peaks to decay at a rate determined by the Gaussian width and is identified as the Debye-Waller factor [32, 52].

A computational challenge associated with Eq. (3.34) is that, at low temperatures, the presence of many higher-order peaks requires high spatial resolution to accurately resolve the corresponding features. In [52], an analysis of the energy contributions from these peaks demonstrated that the excess free energy is primarily concentrated in the first few peaks. This finding suggests that truncating the correlation function to include only the lower-frequency modes is a reasonable approximation. This insight led to the formulation of the correlation function used in the XPFC method, proposed in [51], which serves as one of the defining features of the model.

In the XPFC method, the two-point correlation function is defined in reciprocal space using one or more Gaussian peaks, each corresponding to a symmetry plane of the crystal lattice. Each Gaussian is characterized by three parameters: its position, height and width. The position is determined by the $\boldsymbol{k}$-vector associated with a symmetry plane, typically constructed from a subset of the smallest reciprocal lattice vectors that define the target crystal structure. For a planar spacing of λ_i, the corresponding wave vector is given by $k_i = 2\pi/\lambda_i$. The width parameter, α_i, which is proportional to the interface width, influences both the elastic and surface energy properties [54]. Based on this, the Gaussian function corresponding to the i'th peak is given by

$$\hat{g}_{2,i}(k) = \exp\left(-\frac{(k - k_i)^2}{2\alpha_i^2}\right) \tag{3.35}$$

The use of a Gaussian function is motivated by the presence of interfaces, defects and strains in the crystal structure, where the system is no longer accurately represented by perfect Dirac peaks, as in Eq. (3.34). Furthermore, following [52], the height of the peaks is modulated by a Debye–Waller-like factor that accounts for temperature effects through the effective temperature parameter, σ_v. Thus, the full correlation function for the i'th peak is given by

$$\hat{C}_{2,i}(k) = \hat{a}_i \hat{g}_{2,i}(k) = \exp\left(-\frac{\sigma_v^2 k_i^2}{2\rho_i \beta_i}\right) \exp\left(-\frac{(k - k_i)^2}{2\alpha_i^2}\right) \tag{3.36}$$

where β_i is the number of planes within a given crystal family and ρ_i is the atomic density of those planes. The factor $2\rho_i\beta_i/k_i^2$ acts as an effective transition temperature, characterizing the thermal sensitivity of the corresponding reciprocal mode [54].

For multiple symmetry planes, the full two-point correlation function is defined as the loci of all individual peaks, given by

$$\hat{C}_2(k) = \max_i \left[\hat{C}_{2,i}(k)\right] \tag{3.37}$$

and is used to avoid peak broadening or shifts that may arise from summation, which could otherwise alter the phase stability [52].

3.3.1 Directional correlation function

In all previous discussions on the correlation function, the focus has been on ensuring directional invariance. There are cases, however, where a directionally dependent correlation function is desirable — for example, to identify crystal orientations or to apply an artificial pressure differential across grain boundaries.

Using a formulation similar to that of Eq. (3.37), a directional two-point correlation function can be constructed to energetically favor a specific crystallographic structure and direction. An energy term incorporating such a directional correlation function was introduced in [55], where the directional free energy is defined as

$$F_{dir} = -\frac{k_B T \rho_{ref}}{2} \int d\boldsymbol{r} d\boldsymbol{r}' n(\boldsymbol{r}) H_2(\boldsymbol{r}, \boldsymbol{r}') n(\boldsymbol{r}') \tag{3.38}$$

which is analogous to the excess energy term in Eq. (3.28). In this case, however, the kernel $H_2(\boldsymbol{r}, \boldsymbol{r}')$ is directional, such that $H_2(\boldsymbol{r}, \boldsymbol{r}') = H_2(\boldsymbol{r} - \boldsymbol{r}') \neq H_2(|\boldsymbol{r} - \boldsymbol{r}'|)$. The Fourier transform of H_2 is defined as

$$\hat{H}_2(\boldsymbol{k}) = \max_i \left[h_i \exp\left(-\frac{|\boldsymbol{k} - \boldsymbol{k}_i|}{2\gamma_i^2} \right) \right] \tag{3.39}$$

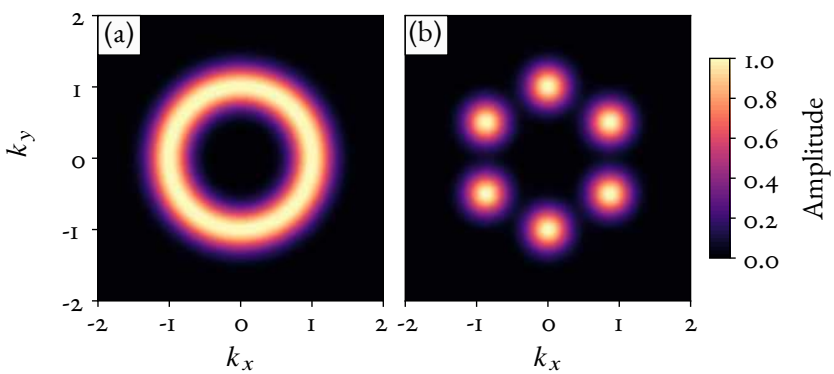

Fig. 3.9: Examples of (a) $\hat{C}_2$ as defined by Eq. (3.37) for a single mode and (b) $\hat{H}_2$ as defined by Eq. (3.39) for the lowest reciprocal vectors of a triangular phase. The inverse Fourier transform of these functions are shown in Fig. 3.10.

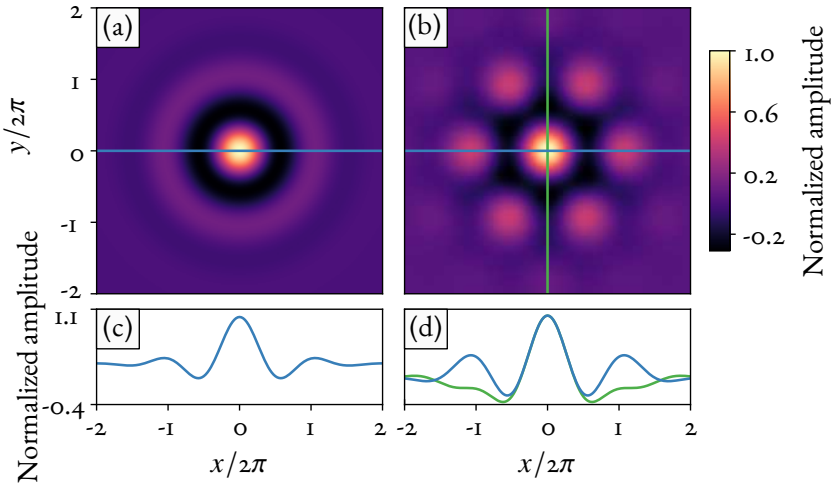

Fig. 3.10: (a) Inverse Fourier transform of $\hat{C}_2$ and (b) $\hat{H}_2$, both shown in Fig. 3.9, with the corresponding density profiles along the indicated lines presented in (c) and (d), respectively. The amplitude is normalized to the maximum value.

where h_i is the peak height, γ_i is the width and $\boldsymbol{k}_i$ represents the target reciprocal vector. The differences between $\hat{C}_2$ and $\hat{H}_2$ are illustrated in Fig. 3.9 for correlation functions that stabilize a triangular phase, while their inverse Fourier transforms are shown in Fig. 3.10. These can be compared to the resulting triangular phase shown in Fig. 3.4(b).

3.3.2 Wavelet filtering

Both the non-directional and directional XPFC correlation functions can be used to identify crystalline phases or even individual crystals. While the non-directional correlation function, Eq. (3.37), is sensitive to the crystal structure only, the directional correlation function, Eq. (3.39), is also sensitive to orientation. These properties can be used to identify regions that match a specific crystal structure and orientation by applying the wavelet transform, following

$$\xi = (X_2 * n)^+ * G \tag{3.40}$$

where $*$ denotes a convolution, G is a Gaussian smoothing kernel and X_2 denotes either C_2 or H_2. When identifying crystal phases, $X_2 = C_2$ is used, whereas $X_2 = H_2$ is employed to detect crystals with specific orientations. Furthermore, $(\cdot)^+$ denotes the positive part, where negative values are set to zero. This prevents negative values from canceling out positive contributions when applying the smoothing kernel. As a result, the application of Eq. (3.40) yields high values (or unity after normalization) at positions where the local structure matches that of X_2 and low values (or zero after normalization) where it does not.

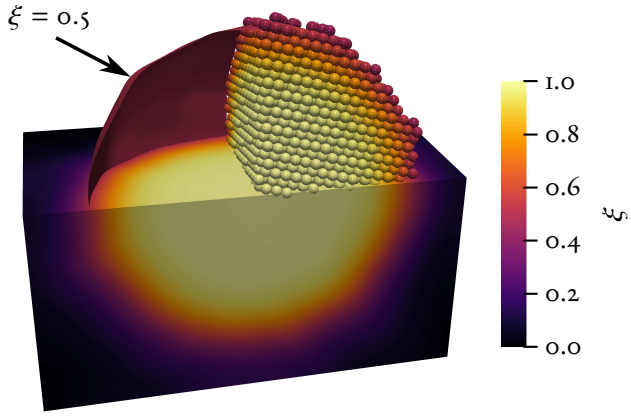

Fig. 3.11: Example of the normalized phase field ξ, its $\xi = 0.5$ contour surface and an atomistic representation of a spherical particle surrounded by a liquid phase.

An example of the application of Eq. (3.40), shown after normalization, is presented in Fig. 3.11. The figure illustrates a region forming a spherical particle, represented through the extracted phase field obtained from Eq. (3.40), its corresponding contour surface and an atomistic representation of the peak positions. As seen in Fig. 3.11, the normalized phase field ξ offers a method for defining the grain boundary via its contour surface — for example, by selecting $\xi = 0.5$.

3.4 Numerical implementation using the spectral method

One of the key advantages of the PFC method is its numerical efficiency, much of which stems from the use of spectral methods. These methods enable efficient parallelization, for example, on GPUs. However, spectral schemes typically require periodic domains. In cases where non-periodic boundary conditions are needed, alternative approaches such as the finite element method (FEM) [56] or finite difference methods [57] can be employed.

Spectral methods are conceptually similar to FEM in that both utilize form functions to describe spatial properties. Specifically, they are both types of weighted residual methods for solving partial differential equations. Unlike FEM, however, where the form functions are localized within elements, spectral methods employ global form functions that span the entire domain. This distinction leads to different advantages and limitations: spectral methods are highly efficient for structured, periodic domains, whereas FEM is well suited for handling complex geometries [58].

One of the most widely used spectral methods is the Fourier spectral method, whose popularity stems from the efficiency of the Fast Fourier Transform (FFT) algorithm. Moreover,

many physical problems naturally exhibit periodic behavior, making the periodicity requirement nonrestrictive in practice.

To apply the spectral method, the time evolution equation — such as that given in Eq. (3.18) — must be expressed in reciprocal space. Various discretization schemes can be employed, with the most straightforward one presented in Sec. 3.4.1. An alternative formulation is presented in [59] and was employed in Paper A.

3.4.1 Time integration using the semi-implicit method

In the semi-implicit scheme, linear terms are treated implicitly to reduce stability constraints, while nonlinear terms are handled explicitly to avoid the computational cost of solving nonlinear equations at each time step [60]. This approach is commonly used in the context of spectral methods [58].

To begin, Eq. (3.28) is inserted into Eq. (3.18), allowing the functional derivative to be evaluated as

$$\frac{\delta F[n]}{\delta n} = k_B T \rho_{ref} \left(n - \frac{1}{2} n^2 + \frac{1}{3} n^3 - C_2 * n \right) \tag{3.41}$$

By substituting Eq. (3.41) into Eq. (3.18), and then applying the Fourier transform, the evolution equation in reciprocal space is obtained as

$$\frac{\partial \hat{n}}{\partial t} = -M k_B T \rho_{ref} k^2 \left[\hat{n} - \frac{1}{2} \widehat{n^2} + \frac{1}{3} \widehat{n^3} - \hat{C}_2 \hat{n} \right] \tag{3.42}$$

where $\widehat{n^i}$ denotes the Fourier transform of n^i. Furthermore, the convolution theorem states that the Fourier transform of a convolution is equal to the product of the individual Fourier transforms, i.e., $\mathcal{F}\{f * g\} = \hat{f}\,\hat{g}$. Applying the semi-implicit scheme to Eq. (3.42) then yields

$$\frac{\hat{n}^{t+1} - \hat{n}^t}{\Delta t} = -\beta \left[\hat{n}^{t+1} - \frac{1}{2} \widehat{n^2}^t + \frac{1}{3} \widehat{n^3}^t - \hat{n}^{t+1} \hat{C}_2 \right] \tag{3.43}$$

where Δt is the time step size and $\beta = M k_B T \rho_{\text{ref}} k^2$. Rearranging Eq. (3.43), the final time-marching scheme is obtained as

$$\hat{n}^{t+1} = \frac{\hat{n}^t + \Delta t \beta \frac{1}{2} \widehat{n^2}^t - \Delta t \beta \frac{1}{3} \widehat{n^3}^t}{1 + \Delta t \beta (1 - \hat{C}_2)} \tag{3.44}$$

Eq. (3.44) can be used to efficiently simulate processes such as the growth of a polycrystal, as illustrated in Fig. 3.12. In this example, small particles are initially seeded and allowed to grow until the entire domain becomes crystallized. The resulting grain boundary network, extracted using Eq. (3.40), is shown in Fig. 3.12(d).

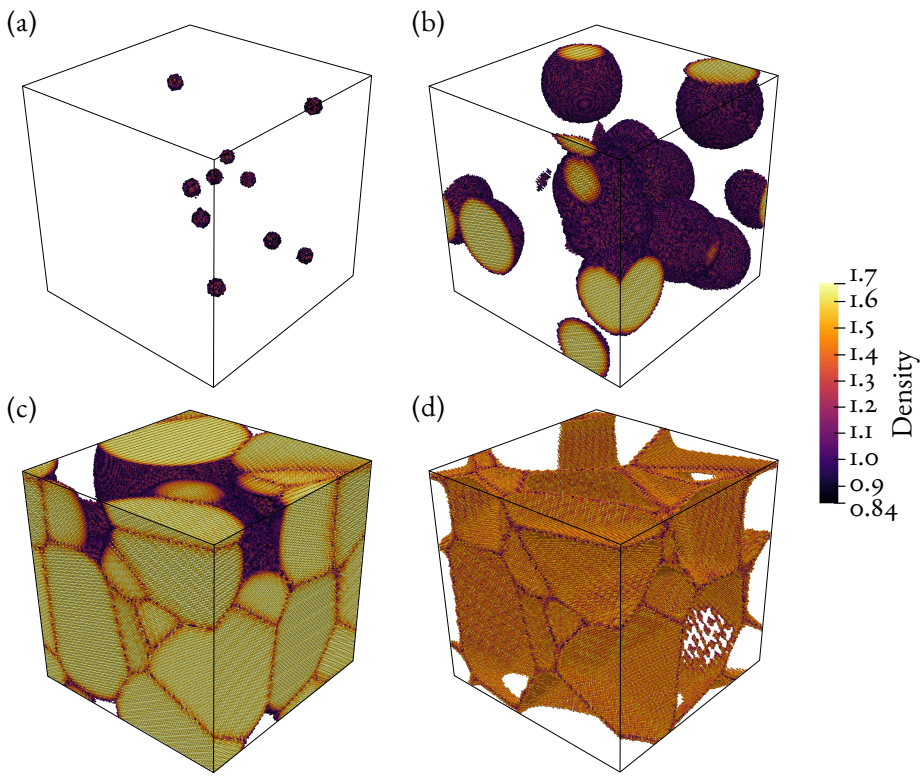

Fig. 3.12: (a)–(d) Growth of an FCC polycrystal, illustrating the formation and evolution of multiple grains over time. In (d), the final grain boundary network is visualized using the wavelet filter defined in Eq. (3.40).

Chapter 4

Overview of appended papers

"Little by little, one travels far."
– Mexican proverb

The papers reproduced at the end of this thesis constitute the core of this thesis. The appended papers, listed in Sec. 4.1 with author contributions detailed in Sec. 4.2, are presented in a logical rather than chronological order. Papers A–C primarily focus on the variation of properties with respect to grain boundary character. Papers C and D investigate migrating grain boundaries, while Paper E compares different models for the stabilization of grain boundary structures in DC bicrystals. As the notation used in the papers varies slightly depending on the reference material, a note on these differences is provided in Sec. 4.3. Some future perspectives and final remarks close this chapter in Sec. 4.4.

4.1 List of appended papers

The appended papers, reproduced at the end of this thesis, are listed below. All except Paper C are based on peer-reviewed publications originally published in their respective journals. To maintain consistency with the thesis format, the papers have been reformatted, which may result in minor deviations from the published versions. Paper C is, at the time of writing, under review. The appended papers are based on the following scientific publications:

Paper A
Kevin Hult Blixt and Håkan Hallberg, *Evaluation of grain boundary energy, structure and stiffness from phase field crystal simulations*, Modelling and Simulation in Materials Science and Engineering 30 (2022) 014002.

Paper B
Håkan Hallberg and Kevin Hult Blixt, *Multiplicity of grain boundary structures and related energy variations*, Materials Today Communications 38 (2024) 107724.

Paper C
Kevin Hult Blixt and Håkan Hallberg, *Phase Field Crystal Modeling of Grain Boundary Migration: Mobility, Energy and Structural Variability*, Under review

Paper D
Kevin Hult Blixt and Håkan Hallberg, *Grain boundary and particle interaction: Enveloping and pass-through mechanisms studied by 3D phase field crystal simulations*, Materials & Design 220 (2022) 110845.

Paper E
Kevin Hult Blixt and Håkan Hallberg, *Phase field crystal modeling of grain boundary structures in diamond cubic systems*, Physical Review Materials 8 (2024) 033606.

4.2 Own contribution

The papers appended to this thesis were all conceptualized and prepared with substantial involvement from the author of this thesis. For papers A and B, key contributions were made to the methodology, implementation, data analysis and manuscript preparation. For Papers C, D and E, the author led the conceptualization, execution and primary writing, but still in close collaboration with the co-author.

4.3 A note on notation

Slight variations in notation occur throughout the appended papers. For clarity, the different notations used for key properties are summarized in Tab. 4.1.

Tab. 4.1: Variations in notation for equivalent parameters used across the appended papers and in Chap. 3. Here, $\mathcal{F}(a)$ denotes the Fourier transform of a.

Property	Chap. 3	Paper A	Paper B	Paper C	Paper D	Paper E
Density field	n	ψ	n	n	ψ	n
$\mathcal{F}(a)$	$\hat{a}$	$\widetilde{a}_{\boldsymbol{k}}$	$\widetilde{a}_k$	$\tilde{a}_k$	a_k	$\hat{a}$
$\mathcal{F}(a^i)$	$\widehat{a^i}$		$\widetilde{a}^i_k$	$\widetilde{(a^i)}_k$	$(a^i)_k$	-

4.4 Future perspectives and final remarks

From the research presented in Papers A–E, it is clear that the study of grain boundaries is not a straightforward endeavor, even in the relatively simple case of single-component bicrystals. For instance, the energy variations shown in Papers A and B show that not only are the five macroscopic DOF important, but microscopic variations also play a significant role. The interplay between microscopic and mesoscopic DOF, however, was not fully explored and represents a promising direction for future research.

Furthermore, the present work focuses exclusively on STGBs, which represent only a small subset of the full range of possible grain boundary orientations. Understanding how grain boundary energy and related properties vary across more general boundary types is essential — particularly in the context of grain boundary migration, as explored in Paper C — since mixed boundaries may exhibit distinct migration behaviors, such as the formation of kinked or stepped structures [61]. Additionally, the different migration regimes observed in Paper C merit further investigation to clarify the underlying mechanisms governing such behavior. Extending the analysis to a broader range of grain boundary types would also be directly relevant to the studies presented in Papers D and E.

Another important consideration is the extension of the investigation from bicrystals to systems containing multiple grains. This would allow for the study of network constraints, such as those imposed by triple junctions, which play a critical role in grain growth. Although such effects are highly relevant, they were not addressed in the appended papers and represent a valuable opportunity for future research and for which the PFC method could be well suited.

To study more general boundaries and polycrystals, however, larger system sizes are required — especially when employing periodic boundary conditions. The largest systems studied in this work were those presented in Paper D, comprising approximately 2.5×10^6

atoms. A natural step toward enabling even larger domains is to utilize increased computational resources, for example, through multi-GPU setups. Alternatively, the computational cost can be reduced by employing a coarse-grained representation of the density field, as done in the Amplitude PFC (APFC) method introduced in [62]. This approach, though efficient, often sacrifices accuracy. Recent developments, such as the model proposed in [63], attempt to combine the strengths of both APFC and PFC approaches to achieve improved accuracy in key properties, including grain boundary energy, and may prove to be a promising direction for PFC simulations of larger domains.

Another approach to increasing domain size is to relax the requirement of periodic boundary conditions. This, however, is not possible with the Fourier spectral method used in this thesis. Instead, alternative methods capable of handling non-periodic boundary conditions — such as FEM — must be employed. The use of FEM for PFC simulations was demonstrated in [64], although periodic boundary conditions were still applied in this specific case. In addition, [63] introduces a real-space convolution-based method for applying Dirichlet boundary conditions, offering a promising avenue for extending PFC simulations to non-periodic domains.

Furthermore, in the application of the XPFC method in Papers B–D, little consideration was given to the precise parameter selection for the correlation function. In fact, variations in peak amplitude and width are known to influence the relative elastic properties, as demonstrated in [65]. Despite this, the estimated grain boundary energies were found to be reasonable, suggesting that the exact parameter choice is not critical, all things considered.

An important consideration in all studies — particularly in Paper C — is the ability to clearly define atomic positions, which is not a straightforward task within the PFC framework. One potential approach to address this problem is to employ the vacancy PFC (VPFC) method introduced in [66], in which negative values in the density field are energetically penalized. The VPFC formulation has also been shown to improve the stabilization of certain defects, such as stacking faults [67]. However, before this model can be applied to studies of grain boundary migration, the grain boundary energy would first need to be reevaluated within the VPFC framework.

Finally, the study of more complex systems may also prove fruitful, as demonstrated in Paper E, although this remains an initial investigation. Further research is needed to accurately quantify grain boundary energies in such systems. The study presented in Paper E was originally motivated by the aim of exploring the more complex case of multi-species perovskites, inspired by the work presented in [68], which initially appeared to be a promising direction. However, the model proposed in [68] was only shown to stabilize a single unit cell. When extended to polycrystalline configurations, the resulting defect structures were not physically plausible. Addressing this issue would have required the introduction of additional interspecies interaction potentials. Consequently, the focus was first narrowed to the Zincblende structure (a two-component DC lattice), as found in Al–Cu alloys, and later further restricted to the comparatively simpler case of single-component DC lattices.

References

[1] C. Herzig and Y. Mishin. *Grain Boundary Diffusion in Metals*, pages 337–366. Springer Berlin, Heidelberg, 2005.

[2] G.S. Rohrer. Grain boundary energy anisotropy: a review. *J. Mater. Sci.*, 46(18):5881–5895, 2011.

[3] W.L. Bragg and J.F. Nye. A dynamical model of a crystal structure. *Proc. R. Soc. Lond. A*, 190:474–481, 1947.

[4] J.D. Bernal and J. Mason. Packing of spheres: Co-ordination of randomly packed spheres. *Nature*, 188(4754):910–911, 1960.

[5] G.D. Scott. Packing of spheres: Packing of equal spheres. *Nature*, 188(4754):908–909, 1960.

[6] N. Hansen. Hall–Petch relation and boundary strengthening. *Scr. Mater.*, 51(8):801–806, 2004.

[7] S. Kondo, T. Mitsuma, N. Shibata, and Y. Ikuhara. Direct observation of individual dislocation interaction processes with grain boundaries. *Science Advances*, 2(11):e1501926, 2016.

[8] K.H. Blixt. Orientation dependant grain boundary diffusion in polycrystals. Master's thesis, Lund University, Department of Construction Sciences, Solid Mechanics, 2020.

[9] H. Bishara, S. Lee, T. Brink, M. Ghidelli, and G. Dehm. Understanding grain boundary electrical resistivity in Cu: The effect of boundary structure. *ACS Nano*, 15(10):16607–16615, 2021.

[10] V.V. Bulatov, B.W. Reed, and M. Kumar. Grain boundary energy function for fcc metals. *Acta Mater.*, 65:161–175, 2014.

[11] F.J. Humphreys, A.D. Rollett, and G.S. Rohrer. *Recrystallization and Related Annealing Phenomena*. Elsevier, Oxford, 3 edition, 2017.

[12] E. Hersent, K. Marthinsen, and E. Nes. The effect of solute atoms on grain boundary migration: A solute pinning approach. *Metall. Mater. Trans. A*, 44(7):3364–3375, 2013.

[13] T. Watanabe. Grain boundary engineering: historical perspective and future prospects. *J. Mater. Sci.*, 46(12):4095–4115, 2011.

[14] W.W. Mullins. Capillarity-induced surface morphologies. *Interface Sci.*, 9(1):9–20, 2001.

[15] C. Herring. Surface tension as a motivation for sintering. In W.E. Kingston, editor, *The Physics of Powder Metallurgy*, pages 143–179. McGraw-Hill, New York, 1951.

[16] F. Abdeljawad, S.M. Foiles, A.P. Moore, A.R. Hinkle, C.M. Barr, N.M. Heckman, K. Hattar, and B.L. Boyce. The role of the interface stiffness tensor on grain boundary dynamics. *Acta Mater.*, 158:440–453, 2018.

[17] R.D. Moore, T. Beecroft, G.S. Rohrer, C.M. Barr, E.R. Homer, K. Hattar, B.L. Boyce, and F. Abdeljawad. The grain boundary stiffness and its impact on equilibrium shapes and boundary migration: Analysis of the $\Sigma 5$, 7, 9, and 11 boundaries in Ni. *Acta Mater.*, 218:117220, 2021.

[18] D. Du, H. Zhang, and D.J. Srolovitz. Properties and determination of the interface stiffness. *Acta Mater.*, 55(2):467–471, 2007.

[19] O. Chirayutthanasak, R. Sarochawikasit, S. Khongpia, T. Okita, S. Dangtip, G.S. Rohrer, and S. Ratanaphan. Universal function for grain boundary energies in bcc metals. *Scr. Mater.*, 240:115821, 2024.

[20] M. Yang, L. Wang, and W. Yan. Phase-field modeling of grain evolutions in additive manufacturing from nucleation, growth, to coarsening. *npj Comput. Mater.*, 7(1):56, 2021.

[21] P. Staublin, A. Mukherjee, J.A. Warren, and P.W. Voorhees. Phase-field model for anisotropic grain growth. *Acta Mater.*, 237:118169, 2022.

[22] H. Hallberg and V.V. Bulatov. Modeling of grain growth under fully anisotropic grain boundary energy. *Modell. Simul. Mater. Sci. Eng.*, 27(4):045002, 2019.

[23] D.L. Olmsted, E.A. Holm, and S.M. Foiles. Survey of computed grain boundary properties in face-centered cubic metals—II: Grain boundary mobility. *Acta Mater.*, 57(13):3704–3713, 2009.

[24] A. Bhattacharya, Y. Shen, C.M. Hefferan, S.F. Li, J. Lind, R.M. Suter, C.E. Krill, and G.S. Rohrer. Grain boundary velocity and curvature are not correlated in Ni polycrystals. *Science*, 374(6564):189–193, 2021.

[25] F.P. Buff, R.A. Lovett, and F.H. Stillinger. Interfacial density profile for fluids in the critical region. *Phys. Rev. Lett.*, 15:621–623, 1965.

[26] M.P.A. Fisher, D.S. Fisher, and J.D. Weeks. Agreement of capillary-wave theory with exact results for the interface profile of the two-dimensional ising model. *Phys. Rev. Lett.*, 48:368–368, 1982.

[27] J.J. Hoyt, M. Asta, and A. Karma. Method for computing the anisotropy of the solid-liquid interfacial free energy. *Phys. Rev. Lett.*, 86:5530–5533, 2001.

[28] Z.T. Trautt and M. Upmanyu. Direct two-dimensional calculations of grain boundary stiffness. *Scr. Mater.*, 52(11):1175–1179, 2005.

[29] S.M. Foiles and J.J. Hoyt. Computation of grain boundary stiffness and mobility from boundary fluctuations. *Acta Mater.*, 54(12):3351–3357, 2006.

[30] E.A. Padston. *Structure and Dynamics of Colloidal Grain Boundaries*. PhD thesis, Harvard University, Cambridge, Massachusetts, 2018.

[31] R.E. Smallman and A.H.W. Ngan. *Modern Physical Metallurgy*. Butterworth-Heinemann, Oxford, 8 edition, 2014.

[32] C. Kittel. *Introduction to Solid State Physics*. John Wiley & Sons, 8 edition, 2005.

[33] A. Rajabzadeh, F. Mompiou, M. Legros, and N. Combe. Elementary mechanisms of shear-coupled grain boundary migration. *Phys. Rev. Lett.*, 110:265507, 2013.

[34] P.R. Cantwell, M. Tang, S.J. Dillon, J. Luo, G.S. Rohrer, and M.P. Harmer. Grain boundary complexions. *Acta Mater.*, 62:1–48, 2014.

[35] H. Ibach and H. Lüth. *Solid-State Physics: An Introduction to Principles of Materials Science*. Springer Berlin, Heidelberg, 4 edition, 2009.

[36] K.R. Elder, N. Provatas, J. Berry, P. Stefanovic, and M. Grant. Phase-field crystal modeling and classical density functional theory of freezing. *Phys. Rev. B*, 75:64–107, 2007.

[37] N. Provatas and K. Elder. *Phase-Field Methods in Materials Science and Engineering*. John Wiley & Sons, 2010.

[38] K.R. Elder, M. Katakowski, M. Haataja, and M. Grant. Modeling elasticity in crystal growth. *Phys. Rev. Lett.*, 88:245701, 2002.

[39] J. Swift and P.C. Hohenberg. Hydrodynamic fluctuations at the convective instability. *Phys. Rev. A*, 15:319–328, 1977.

[40] V. Serov. *Fourier Series, Fourier Transform and Their Applications to Mathematical Physics*. Springer, 1 edition, 2017.

[41] S. van Teeffelen, R. Backofen, A. Voigt, and H. Löwen. Derivation of the phase-field-crystal model for colloidal solidification. *Phys. Rev. E*, 79:051404, 2009.

[42] R.W. Balluffi and S.M. Allen. *Kinetics of materials*. Wiley, 2005.

[43] P. Stefanovic, M. Haataja, and N. Provatas. Phase-field crystals with elastic interactions. *Phys. Rev. Lett.*, 96:225504, 2006.

[44] Z.T. Trautt, A. Adland, A. Karma, and Y. Mishin. Coupled motion of asymmetrical tilt grain boundaries: Molecular dynamics and phase field crystal simulations. *Acta Mater.*, 60(19):6528–6546, 2012.

[45] H. Hallberg and K.H. Blixt. Evaluation of nanoscale deformation fields from phase field crystal simulations. *Metals*, 12(10), 2022.

[46] K. Wu and A. Karma. Phase-field crystal modeling of equilibrium bcc-liquid interfaces. *Phys. Rev. B*, 76:184107, 2007.

[47] M. Schmidt, M. Burgis, W.S.B. Dwandaru, G. Leithall, and P. Hopkins. Recent developments in classical density functional theory: Internal energy functional and diagrammatic structure of fundamental measure theory. *Condens. Matter Phys.*, 15:43603, 2012.

[48] D.V. Schroeder. *An introduction to thermal physics*. Oxford University Press, 2021.

[49] H. Emmerich, H. Löwen, R. Wittkowski, T. Gruhn, G.I. Tóth, G. Tegze, and L. Gránásy. Phase-field-crystal models for condensed matter dynamics on atomic length and diffusive time scales: an overview. *Adv. Phys.*, 61(6):665–743, 2012.

[50] T.V. Ramakrishnan and M. Yussouff. First-principles order-parameter theory of freezing. *Phys. Rev. B*, 19:2775–2794, 1979.

[51] M. Greenwood, N. Provatas, and J. Rottler. Free energy functionals for efficient phase field crystal modeling of structural phase transformations. *Phys. Rev. Lett.*, 105:045702, 2010.

[52] M. Greenwood, N. Ofori-Opoku, J. Rottler, and N. Provatas. Modeling structural transformations in binary alloys with phase field crystals. *Phys. Rev. B*, 84:064104, 2011.

[53] A.D. Poularikas. *Handbook of Formulas and Tables for Signal Processing*. CRC Press, 1999.

[54] M. Berghoff and B. Nestler. Phase field crystal modeling of ternary solidification microstructures. *Comput. Condens. Matter*, 4:46–58, 2015.

[55] M. Greenwood, C. Sinclair, and M. Militzer. Phase field crystal model of solute drag. *Acta Mater.*, 60:5752–5761, 2012.

[56] V. Ankudinov. Structural phase-field crystal model for Lennard-Jones pair interaction potential. *Modell. Simul. Mater. Sci. Eng.*, 30(6):064002, 2022.

[57] J. Yang, J. Wang, and Z. Tan. A simple and practical finite difference method for the phase-field crystal model with a strong nonlinear vacancy potential on 3D surfaces. *Comput. Math. Appl.*, 121:131–144, 2022.

[58] J. Shen, T. Tang, and L. Wang. *Spectral Methods*. Springer Berlin, Heidelberg, 2011.

[59] J. Mellenthin, A. Karma, and M. Plapp. Phase-field crystal study of grain-boundary premelting. *Phys. Rev. B*, 78:184110, 2008.

[60] S.B. Biner. *Programming Phase-Field Modeling*. Springer International Publishing, 2017.

[61] R. Hadian, B. Grabowski, C.P. Race, and J. Neugebauer. Atomistic migration mechanisms of atomically flat, stepped, and kinked grain boundaries. *Phys. Rev. B*, 94:165413, 2016.

[62] N. Goldenfeld, B.P. Athreya, and J.A. Dantzig. Renormalization group approach to multiscale simulation of polycrystalline materials using the phase field crystal model. *Phys. Rev. E*, 72:020601, 2005.

[63] M. Punke and M. Salvalaglio. Hybrid-PFC: Coupling the phase-field crystal model and its amplitude-equation formulation. *Comput. Methods Appl. Mech. Eng.*, 436:117719, 2025.

[64] E. Asadi and M.A. Zaeem. Quantifying a two-mode phase-field crystal model for BCC metals at melting point. *Comput. Mater. Sci*, 105:101–109, 2015.

[65] J. Holmberg-Kasa, P.A.T. Olsson, and M. Fisk. Investigating elastic deformation of ordered precipitates by ab initio-informed phase-field crystal modeling. *Metals*, 14(12), 2024.

[66] P.Y. Chan, N. Goldenfeld, and J. Dantzig. Molecular dynamics on diffusive time scales from the phase-field-crystal equation. *Phys. Rev. E*, 79:035701, 2009.

[67] J. Berry, N. Provatas, J. Rottler, and C.W. Sinclair. Defect stability in phase-field crystal models: Stacking faults and partial dislocations. *Phys. Rev. B*, 86:224112, 2012.

[68] E. Alster, D. Montiel, K. Thornton, and P.W. Voorhees. Simulating complex crystal structures using the phase-field crystal model. *Phys. Rev. Mater.*, 1:060801, 2017.

Bibliography

[1] P. Škarvada, P. Tománek, P. Koktavý, R. Macků, J. Šicner, M. Vondra, D. Dallaeva, S. Smith, and L. Grmela. A variety of microstructural defects in crystalline silicon solar cells. *Appl. Surf. Sci.*, 312:50–56, 2014.

[2] D. Kohler, A. Zuschlag, and G. Hahn. On the origin and formation of large defect clusters in multicrystalline silicon solar cells. *Sol. Energy Mater. Sol. Cells*, 120:275–281, 2014.

[3] R.D. Kamachali. A model for grain boundary thermodynamics. *RSC Adv.*, 10(45):26728–26741, 2020.

[4] V.W.L. Chan, N. Pisutha-Arnond, and K. Thornton. Phase-field crystal model for a diamond-cubic structure. *Phys. Rev. E*, 91(5):053305, 2015.

[5] S.V. Rodriguez, M. Frick, N. Quitoriano, N. Ofori-Opoku, N. Provatas, and K.H. Bevan. Capturing dislocation half-loop formation and dynamics in epitaxial growth atomistically at diffusive time scales. *Materialia*, 20:101253, 2021.

[6] E. Alster, D. Montiel, K. Thornton, and P.W. Voorhees. Simulating complex crystal structures using the phase-field crystal model. *Phys. Rev. Materials*, 1:060801, 2018.

[7] Z. Wang, Z. Liu, and Z. Huang. Angle-adjustable density field formulation for the modeling of crystalline microstructure. *Phys. Rev. B*, 97(18):180102, 2018.

[8] Z. Wang, Z. Liu, W. Duan, and Z. Huang. Control of phase ordering and elastic properties in phase field crystals through three-point direct correlation. *Phys. Rev. E*, 105(4):044802, 2022.

[9] M. De Donno, L. Benoit–Maréchal, and M. Salvalaglio. Amplitude expansion of the phase-field crystal model for complex crystal structures. *Phys. Rev. Materials*, 7(3):033804, 2023.

[10] M. Seymour and N. Provatas. Structural phase field crystal approach for modeling graphene and other two-dimensional structures. *Phys. Rev. B*, 93(3):035447, 2016.

[11] M.C. Rechtsman, F.H. Stillinger, and S. Torquato. Synthetic diamond and wurtzite structures self-assemble with isotropic pair interactions. *Phys. Rev. E*, 75(3):031403, 2007.

[12] M. Lavrskyi, H. Zapolsky, and A.G. Khachaturyan. Quasiparticle approach to diffusional atomic scale self-assembly of complex structures: from disorder to complex crystals and double-helix polymers. *npj Comput. Mater.*, 2:15013, 2016.

[13] F.H. Stillinger and T.A. Weber. Computer simulation of local order in condensed phases of silicon. *Phys. Rev. B*, 31(8):5262–5271, 1985.

[14] M. Greenwood, N. Provatas, and J. Rottler. Free energy functionals for efficient phase field crystal modeling of structural phase transformations. *Phys. Rev. Lett.*, 105(4):045702, 2010.

[15] K.H. Blixt and H. Hallberg. Grain boundary and particle interaction: Enveloping and pass-through mechanisms studied by 3D phase field crystal simulations. *Mater. Des.*, 220:110845, 2022.

[16] K.H. Blixt and H. Hallberg. Evaluation of grain boundary energy, structure and stiffness from phase field crystal simulations. *Modell. Simul. Mater. Sci. Eng.*, 30:014002, 2022.

[17] J. Hickman and Y. Mishin. Extra variable in grain boundary description. *Phys. Rev. Materials*, 1(1):010601, 2017.

[18] H. Hallberg and K.H. Blixt. Multiplicity of grain boundary structures and related energy variations. *Mater. Today Commun.*, 38:107724, 2024.

[19] M. Kohyama. Structure and energies of symmetrical ⟨001⟩ tilt grain boudaries in silicon. *Phys. Stat. Sol. (b)*, 141(1):71–83, 1987.

[20] T. Yokoi, Y. Noda, A. Nakamura, and K. Matsunaga. Neural-network interatomic potential for grain boundary structures and their energetics in silicon. *Phys. Rev. Materials*, 4(1):014605, 2020.

[21] M. Guziewski, A.D. Banadaki, S. Patala, and S.P. Coleman. Application of Monte Carlo techniques to grain boundary structure optimization in silicon and silicon-carbide. *Comput. Mater. Sci.*, 182:109771, 2020.

[22] C. Kohler. Atomistic modelling and of structures and of tilt and grain and boundaries and antiphase and boundaries in β-Silicon Carbide. *Phys. Stat. Sol. (b)*, 234(2):522–540, 2001.

[23] M.G. Tsoutsouva, P.E. Vullum, K. Adamczyk, M. Di Sabatino, and G. Stokkan. Interfacial atomic structure and electrical activity of nano-facetted CSL grain boundaries in high-performance multi-crystalline silicon. *J. Appl. Phys.*, 127(12):125109, 2020.

[24] M. Kohyama, R. Yamamoto, and M. Doyama. Structure and energies of symmetrical ⟨011⟩ tilt grain boundaries in silicon. *Phys. Stat. Sol. (b)*, 137(1):11–20, 1986.

[25] L. Wang, W. Yu, and S. Shen. Revisiting the structures and energies of silicon ⟨110⟩ symmetric tilt grain boundaries. *J. Mater. Res.*, 34(6):1021–1033, 2019.

[26] L. Sun, M.A.L. Marques, and S. Botti. Direct insight into the structure-property relation of interfaces from constrained crystal structure prediction. *Nat. Commun.*, 12(1):811, 2021.

[27] J. Tersoff. New empirical approach for the structure and energy of covalent systems. *Phys. Rev. B*, 37(12):6991–7000, 1988.

[28] K.R. Elder, M. Katakowski, M. Haataja, and M. Grant. Modeling elasticity in crystal growth. *Phys. Rev. Lett.*, 88(24):245701, 2002.

[29] A. Jaatinen and T. Ala-Nissila. Extended phase diagram of the three-dimensional phase field crystal model. *J. Phys. Condens. Matter*, 22:205402, 2010.

[30] J. Berry, N. Provatas, J. Rottler, and C. W. Sinclair. Defect stability in phase-field crystal models: Stacking faults and partial dislocations. *Phys. Rev. B*, 86(22):224112, 2012.

[31] P.Y. Chan, N. Goldenfeld, and J. Dantzig. Molecular dynamics on diffusive time scales from the phase-field-crystal equation. *Phys. Rev. E*, 79(3):035701(R), 2009.